Conformal piezoelectric systems for clinical and experimental characterization of soft tissue biomechanics

Canan Dagdeviren[1,2][†], Yan Shi[3,4,5], Pauline Joe[1,2], Roozbeh Ghaffari[6], Guive Balooch[7], Karan Usgaonkar[1,2], Onur Gur[8], Phat L. Tran[9], Jessi R. Crosby[9], Marcin Meyer[10], Yewang Su[4,5,11], R. Chad Webb[1,2], Andrew S. Tedesco[12], Marvin J. Slepian[9,13], Yonggang Huang[4,5] and John A. Rogers[1,2,8,14]*

Mechanical assessment of soft biological tissues and organs has broad relevance in clinical diagnosis and treatment of disease. Existing characterization methods are invasive, lack microscale spatial resolution, and are tailored only for specific regions of the body under quasi-static conditions. Here, we develop conformal and piezoelectric devices that enable *in vivo* measurements of soft tissue viscoelasticity in the near-surface regions of the epidermis. These systems achieve conformal contact with the underlying complex topography and texture of the targeted skin, as well as other organ surfaces, under both quasi-static and dynamic conditions. Experimental and theoretical characterization of the responses of piezoelectric actuator–sensor pairs laminated on a variety of soft biological tissues and organ systems in animal models provide information on the operation of the devices. Studies on human subjects establish the clinical significance of these devices for rapid and non-invasive characterization of skin mechanical properties.

Human skin is the largest organ of the body[1]; its epidermal and dermal layers serve as the external envelope for containment of all viscera, fluids and tissue constituents, as a protective barrier to environmental hazards, pathogens and toxins, as a sensory interface for transduction of physical stimuli—for example, pressure and cold—and as a modulating membrane for control of water, electrolytes and other biochemical mediators[2]. Despite these essential roles, there is much that is unknown about the basic physical properties of the skin, including details related to its responses to mechanical loads. Precise measurements of the elastic modulus of the skin under various conditions can facilitate the assessment of a variety of pathophysiologic conditions[3], may predict reactions to exogenous substances and environmental factors[4,5], can help in gauging the effectiveness of cosmetic products[5] and further establish mechanisms associated with growth, repair and ageing[6–9]. Mechanical properties specifically are centrally important in the diagnosis and treatment of disorders[10] such as scleroderma, Ehlers–Danlos syndrome, psoriasis, eczema, melanoma, and other cutaneous pathologies, all of which involve changes in the elastic modulus of the skin[7,11–14]. Further, the outermost layer of the skin, the stratum corneum (SC; ref. 15), is critical in

mechano-protection[1], somato-sensory reception[16] and thermal regulation[2]. Understanding the mechanical properties of the SC alone is relevant to the design of percutaneous penetration strategies and optimization of topical therapy to treat damaged skin[17].

At present, methods for *in vivo* measurement of the elasticity and physical durability of the skin involve pressure-based suction[18,19], torsion[20,21], traction[22], nanoindentation[23] and ultrasound elastography[24]. Although these techniques can provide important insights into the mechanics of the skin, the measurements typically involve large uncertainties and the associated tools are not amenable to wearable device architectures for continuous monitoring or to non-invasive use on sensitive or highly curved regions.

Here we introduce a set of materials and device designs that allow for *in vivo* measurements of viscoelasticity in the near-surface regions of the epidermis through the use of ultrathin, stretchable networks of mechanical actuators and sensors constructed with nanoribbons of lead zirconate titanate (PZT). Soft, reversible lamination onto the skin enables rapid, quantitative assessment of viscoelastic moduli, with the ability for spatial mapping. Comprehensive experimental and theoretical studies establish that these systems can provide accurate and reproducible measurements of both the

[1]Department of Materials Science and Engineering, Beckman Institute for Advanced Science and Technology, University of Illinois at Urbana-Champaign, Urbana, Illinois 61801, USA. [2]Frederick Seitz Materials Research Laboratory, University of Illinois at Urbana-Champaign, Urbana, Illinois 61801, USA. [3]State Key Laboratory of Mechanics and Control of Mechanical Structures, Nanjing University of Aeronautics & Astronautics, Nanjing 210016, China. [4]Department of Civil and Environmental Engineering, Northwestern University, Evanston, Illinois 60208, USA. [5]Department of Mechanical Engineering, Center for Engineering and Health and Skin Disease Research Center, Northwestern University, Evanston, Illinois 60208, USA. [6]MC10 Inc., Cambridge, Massachusetts 02140, USA. [7]L'Oreal R&I Incubator, Department of Research and Innovation, Clark, New Jersey 07066, USA. [8]Department of Electrical and Computer Engineering, University of Illinois at Urbana-Champaign, Urbana, Illinois 61801, USA. [9]Department of Medicine & Sarver Heart Center, The University of Arizona, Tucson, Arizona 85724, USA. [10]Institute for Materials Science and Max Bergmann Center of Biomaterials, TU Dresden, 01062 Dresden, Germany. [11]Center for Mechanics and Materials, Tsinghua University, Beijing 100084, China. [12]Academy Dermatologist Group Ltd, Tucson, Arizona 85710, USA. [13]Department of BioMedical Engineering, The University of Arizona, Tucson, Arizona 85724, USA. [14]Department of Chemistry and Department of Mechanical Science and Engineering, University of Illinois at Urbana-Champaign, Urbana, Illinois 61801, USA. [†]Present address: The David H. Koch Institute for Integrative Cancer Research, Massachusetts Institute of Technology, Cambridge, Massachusetts 02139, USA. *e-mail: jrogers@illinois.edu

storage and loss moduli for a variety of substrates and conditions. Applications *in vitro* with mock and *ex vivo* skin preparations under varying conditions and *in vivo* on human subjects, collected at various locations over all main regions of body, under both normal conditions and following administration of pharmacological and cosmetic (moisturizing) agents, demonstrate the capabilities. Additional experiments on other organ systems, including different regions of the heart and lung, suggest broad applicability to nearly all parts of the body, and to biomaterials more generally.

Figure 1a and Supplementary Figs 1 and 2 provide schematic diagrams and images of this type of conformal modulus sensor (CMS). The ultrathin architectures of the active elements—together with the serpentine configurations of metal traces that establish electrical connection to them—yield low modulus, stretchable mechanics when supported by a thin elastomer (Ecoflex 00-30, Smooth-On; weight ratio of 1A:1B, 60 kPa, 20 μm thick). The resulting device can directly couple to the surface of the skin or other biological tissues by van der Waals forces alone (Fig. 1b,c). Application and removal of the devices occur non-invasively, over multiple cycles of use (500×), without significant change in measurement accuracy (Fig. 1d,e). The rectangular structures are capacitor-type components, each of which incorporates a layer of piezoelectric material (PZT, 500 nm thick) between bottom (Ti/Pt, 20 nm/300 nm) and top (Cr/Au, 10 nm/200 nm) electrodes, with an encapsulation layer of polyimide (PI). Such elements serve as both mechanical actuators and sensors (Supplementary Note 1). *In vitro* studies with human epithelial keratinocytes demonstrate that the devices are biocompatible. In particular, cell viability studies reveal no evidence of toxicity and the cell culturing process does not change the surface properties (Supplementary Fig. 3).

A CMS module consists of seven actuators (lateral dimensions of $200 \times 1,000\,\mu\text{m}^2$) and six sensors (lateral dimensions of $100 \times 500\,\mu\text{m}^2$), as shown (without elastomer substrate) mounted on an artificial skin surface in Fig. 1b,f,g. Both serpentine interconnections and sensors/actuators (Supplementary Fig. 4) conform to this textured surface, even without the elastomer. The bending stiffness per width ($4.55 \times 10^{-8}\,\text{N m}$) and the position of the neutral mechanical plane (near the middle of PZT layer) can be obtained analytically, as in Supplementary Note 1. For a bending radius as small as 0.3 mm, the maximum strains in PZT and PI are only 0.1% and 1%, respectively. Devices subjected to extensive cycles of stretching (>1,000×) (Supplementary Fig. 5a–d) showed no delamination of the metal/piezoelectric materials from the elastomeric substrate. Measurements indicate stable performance characteristics under hundreds of cycles of application to and removal from the skin (Supplementary Fig. 5e,f). Furthermore, the performance of the related devices is consistent over a range of temperatures (25–35 °C) that are relevant to modulus measurements[25]. The uniaxial failure strain is as high as 30% (Supplementary Fig. 6).

With the device conformally mounted on the skin, application of a sinusoidally varying voltage (angular frequency ω) to a selected actuator induces mechanical motions in the PZT and associated device structures, including the elastomer backing, and, through physical contact, the underlying skin. These motions mechanically couple, through skin and elastomer, to adjacent sensor elements. Detecting the voltage response (amplitude and phase) of each sensor at the actuation frequency determines the extent of this coupling. By neglecting the effects of interfacial shear stress, an approximate theoretical model can be constructed (Supplementary Fig. 7a,b) to describe the response, and to relate it, explicitly, to the mechanical properties of skin. As shown in Supplementary Fig. 7c, the interfaces between the PZT elements and the skin can be treated as interfacial cracks, although there is no delamination between actuator/sensor and elastomer substrate. A constant voltage U_A (the same as the amplitude of the sinusoidally varying voltage used in the experiment) applied to a given element (actuator, A; Fig. 1f) induces

an expansion ($\delta_{\text{active}-A}$) that is six to eight orders of magnitude larger than that of any other element (sensor, S) in the array ($\delta_{A/S}$; see Supplementary Note 3); the latter is therefore negligible, that is,

$$\begin{cases} \delta_{\text{active}-A} = \Delta u \\ \delta_{A/S} = 0 \end{cases}$$

where Δu is obtained analytically as

$$\Delta u = \beta_1 \frac{e_{33}}{c_{33}} U_A \qquad (1)$$

where c_{33} and e_{33} are the elastic and piezoelectric parameters of PZT, respectively, and the dimensionless parameter β_1 depends on the materials and geometries associated with the multilayer structure of the device, but is approximately independent of the modulus of sample under test, provided that this sample has a modulus much smaller than that of actuator (for example, six orders of magnitude difference between PZT and skin). See Supplementary Note 2.

The stress induced by the actuator on each of the other elements in the array can be characterized by its average stress ($p_{S,i}$, for the ith sensor element) according to

$$p_{S,i} = \eta_i \frac{\Delta u \cdot E_{P.S.}}{2a} \qquad (2)$$

where $E_{P.S.}$ and $2a$ represent the storage (elastic) modulus of skin (or, more generally, the substrate under test) and the width of the sensor, respectively. An expression for the dimensionless parameter η_i is given in Supplementary Note 3. The output voltage of the ith element is then obtained as

$$U_{S,i} = \beta_2 \frac{p_{S,i} \cdot h_{PZT}}{e_{33}} \qquad (3)$$

where h_{PZT} represents the thickness of PZT layer, and the dimensionless parameter β_2 depends on the materials and geometries associated with the multilayer structure of the device (Supplementary Note 3). Substitution of equations (1) and (2) into equation (3) leads to

$$U_{S,i} = \alpha_i \frac{h_{PZT}}{2a} \frac{E_{P.S.}}{c_{33}} U_A \qquad (4)$$

where $\alpha_i = \beta_1 \cdot \beta_2 \cdot \eta_i$ decays exponentially with the location of the ith sensor element, that is,

$$\frac{\alpha_i}{\alpha_1} \propto e^{-(i-1)} \qquad (5)$$

Owing to the dynamic nature of measurement process, viscoelastic effects can be important. In general, the dependence of the storage (elastic) modulus on ω can be expressed as a Prony series, according to[26]

$$E_{P.S.}(\omega) = E_\infty \frac{1 - \sum_{i=1}^{N} \frac{g_i}{1 + \tau_i^2 \omega^2}}{1 - \sum_{i=1}^{N} g_i} \qquad (6)$$

where E_∞ is the fully relaxed modulus (when $\omega = 0$), and g_i and τ_i are, respectively, the relaxation ratio and relaxation time in the Prony series. In Supplementary Note 4, the PI layer between the device substrate and PZT actuators/sensors may further suppress viscoelastic effects of the device.

Relaxation times range from microseconds to seconds for skin[27], which are much shorter than those for the constituent materials of the CMS (for example, a relaxation time of hundreds of hours for silicone[28]). For the range of frequencies (100–1,000 Hz) and examined biological samples, we neglect viscoelastic effects in the device. For consistency, we use this same approximation in the control studies described next.
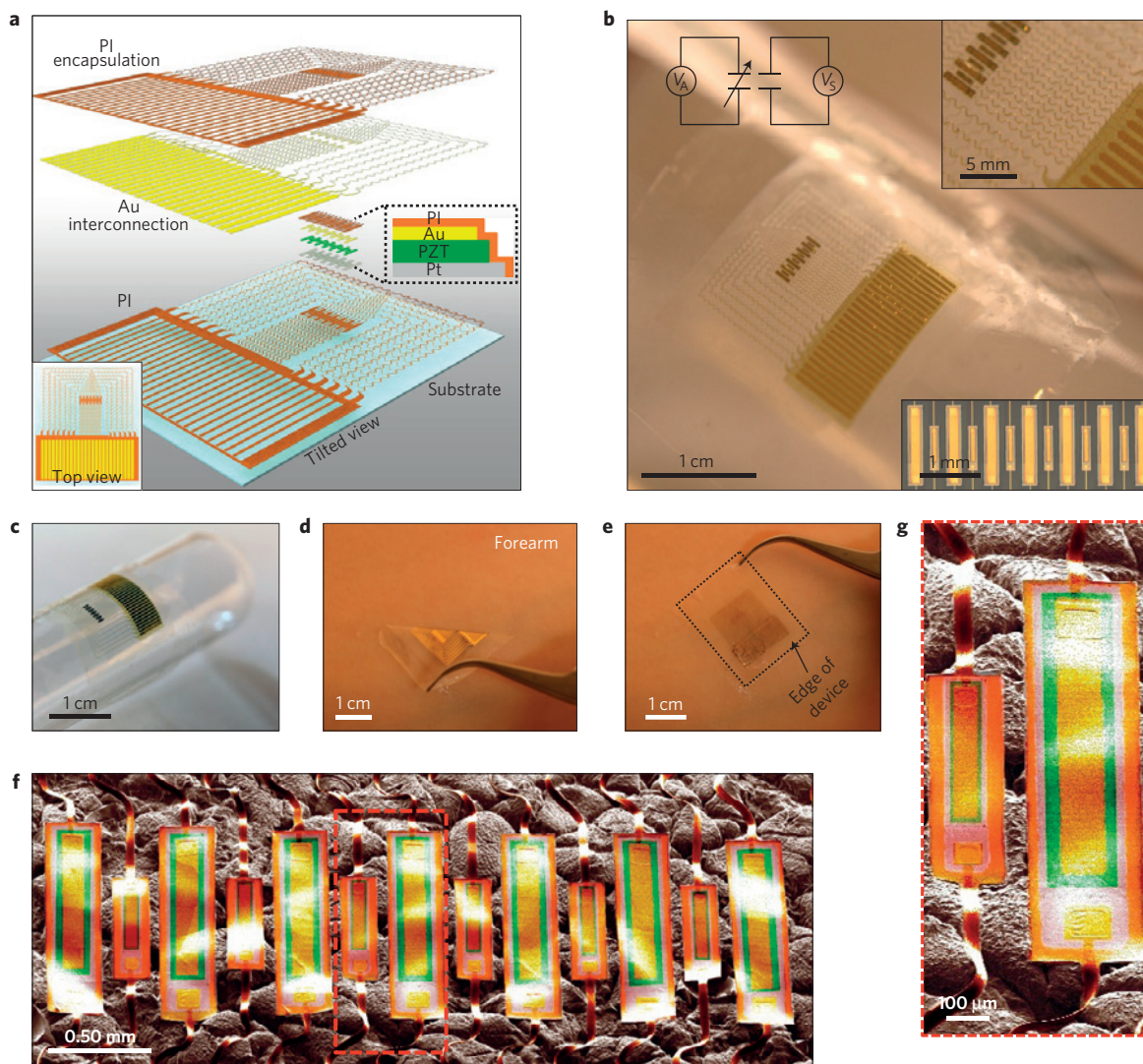
Figure 1 | Thin, compliant modulus sensor (CMS) based on nanoribbons of PZT in arrays of mechanical actuators and sensors. a, Exploded-view schematic illustration of the device, with a top view in the lower-left inset, and a cross-sectional view of actuators and sensors in the black dashed region. **b**, Photograph of a device on a thin silicone substrate. Optical microscope images of the interconnect region (upper-right inset), the actuator/sensor arrays (lower-right inset), and a simple electrical circuit diagram of actuators and sensors (upper-left inset). **c**, Photograph of a device on a cylindrical glass support. **d,e**, Photographs of a device partially (**d**) and fully (**e**) laminated on the skin. **f**, SEM image of a device on an artificial skin sample. **g**, A magnified view of the red dashed region in **f**, where sensor and actuator are on the left and right sides, respectively.

Experiments designed to examine these predicted relationships involved a set of samples of polydimethylsiloxane (PDMS, Sylgard 184, Dow Corning) formulated to yield a range of Young's moduli (Supplementary Fig. 8) relevant to skin and other soft biological tissues. The data recording system consisted of a lock-in amplifier (SR830, Standard Research Systems, USA), a multiplexer (FixYourBoard.com, U802, USA), and a computer for determining both the amplitude of the voltage response of each sensor in the array and the phase shift (δ) relative to the sinusoidal voltage applied the actuator. Measurements at 1,000 Hz show that the amplitudes of the sensor voltages vary linearly with the actuator voltages (Fig. 2a) and with the Young's modulus (separately evaluated using a dynamic mechanical analyser; Q800 DMA at 0 Hz) of the sample under test (Fig. 2b), consistent with equation (4). This linear relation does not hold strictly for samples with extremely low moduli because the previously neglected interfacial shear stresses will become important. The amplitudes decay in an approximately exponential fashion with distance, as expected based on equation (5). The amplitude for each sensor can be used

with equation (4) to define a value of $E_{P.S.}$. The phase shift then defines the loss modulus according to $E_{\text{loss}} = E_{P.S.} \tan(\delta)$, where the loss modulus is given in Supplementary Note 4. Measurements at different actuation frequencies (100 Hz, 500 Hz and 1,000 Hz) yield the frequency dependence of these two moduli (Fig. 2c,d). With the relaxation ratios g_i in the Prony series taken from the literature[29,30], the fully relaxed modulus E_∞ and relaxation times τ_i (for $N = 3$) can be determined from the thirty sensor data points (five sensors on two different PDMS formulations, with fully relaxed moduli of 30 and 1,800 kPa, at three measurement frequencies) via the following relation, which results from equations (4) and (6)

$$U_{S,i} = \alpha_i \frac{h_{\text{PZT}}}{2a} U_A \frac{E_\infty}{c_{33}} \frac{1 - \sum_{i=1}^{N} \frac{g_i}{1 + \tau_i^2 \omega^2}}{1 - \sum_{i=1}^{N} g_i} \qquad (7)$$

(Supplementary Note 4). The fully relaxed moduli agree well with those measured independently by DMA at ∼0 Hz. The τ_i determined in this manner, together with the relaxation ratios g_i,
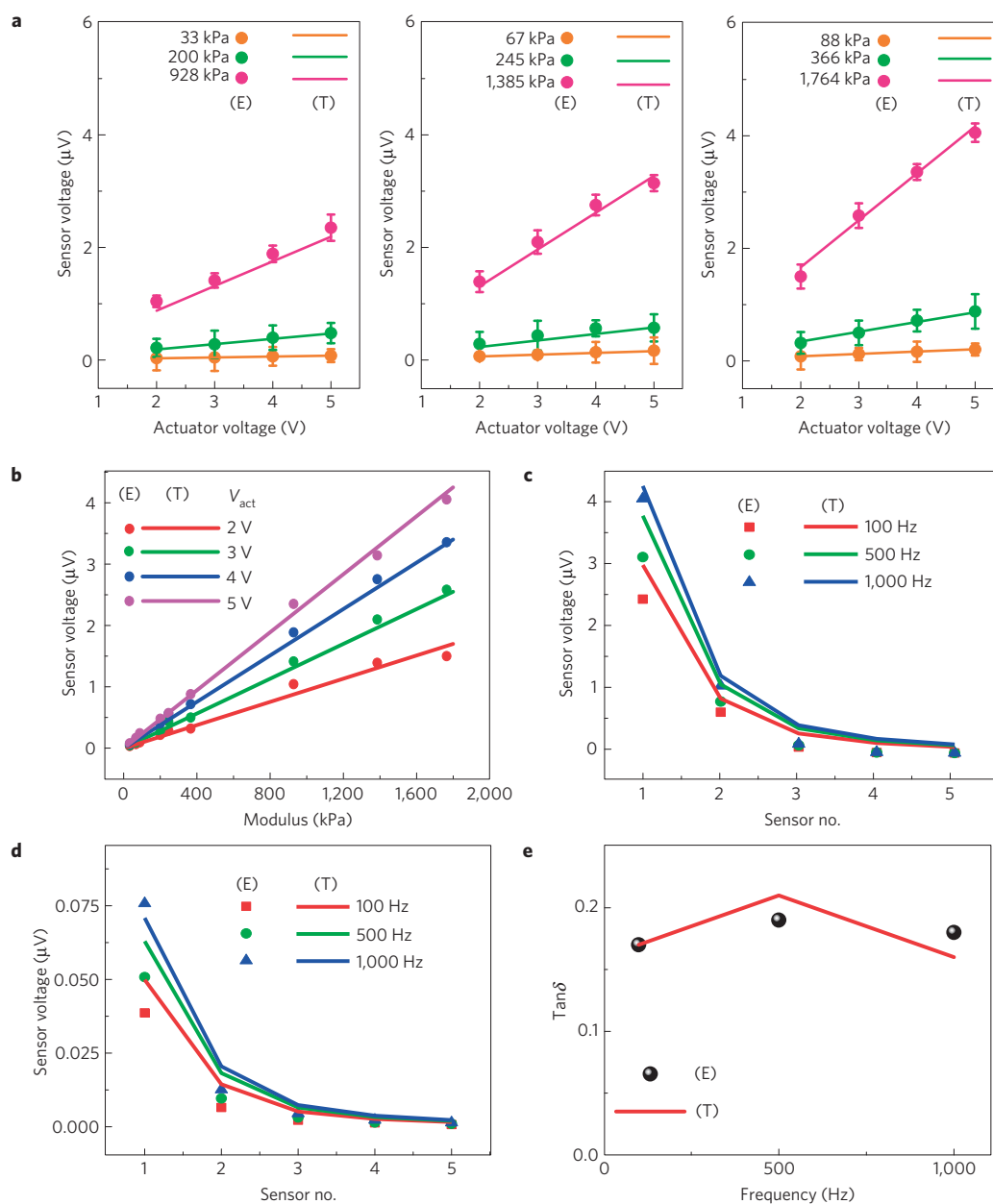
Figure 2 | Experimental and theoretical analysis of the device operation. a, Voltage output of sensor no. 1 (that is, the sensor adjacent to the active actuator) as a function of actuator voltage, measured on nine different PDMS substrates with known moduli, separately evaluated by quasi-static dynamical mechanical analysis as in Supplementary equation (11). Here, and in all other cases, the symbols and lines correspond to experimental (E) and theoretical (T) results, respectively. Error bars correspond to calculated standard error deviation. **b**, Output voltage from sensor no. 1 as a function of the modulus of the substrate under test, for four actuator voltages (V_{act}). **c,d**, Output voltages for each of the different sensors in the array (that is, sensor no. 1, no. 2, and so on) measured during use with two different formulations of PDMS, $E_{PDMS} = 1{,}800$ kPa (**c**) and $E_{PDMS} = 30$ kPa (**d**), at three different frequencies, all at an actuation voltage of 5 V. **e**, Tanδ as a function of actuation frequency.

give the phase shifts δ, which agree well with values determined from experiment (Fig. 2e).

For the Prony series obtained above and an actuation frequency of 1 kHz, the fully relaxed moduli can be obtained in the same way (from equation (7)) for nine different PDMS formulations (Supplementary Fig. 9). All results agree well with those determined independently by DMA at ~0 Hz, as shown in Fig. 2a,b. Consistent with the previous examples, the output voltages are linearly proportional to the modulus of the sample under test, over the entire range, from 30 to 1,800 kPa. Application to the rough surfaces of artificial skin structures formed by moulding these same formulations of PDMS yielded similar results (Supplementary

Fig. 10). Here, also in cases of large-scale curvature, the neutral mechanical plane layout with respect to PZT is important (Supplementary Fig. 11). See Supplementary Note 5.

These findings establish CMS as a versatile tool for characterizing the mechanical properties of soft materials. The following examines use with biomaterials, with a focus on the storage modulus evaluated at a given frequency. As a demonstration of utility with skin, CMS data obtained from *ex vivo* samples reveal the effects of moisturizing agents and hydration state, in systematic experiments that involve measurements before and at various times after application of solutions containing 1% acrylamidomethylpropane sulphonic acid (AMPS), 3% glycerin, and 3% urea. Results for AMPS (supplied by
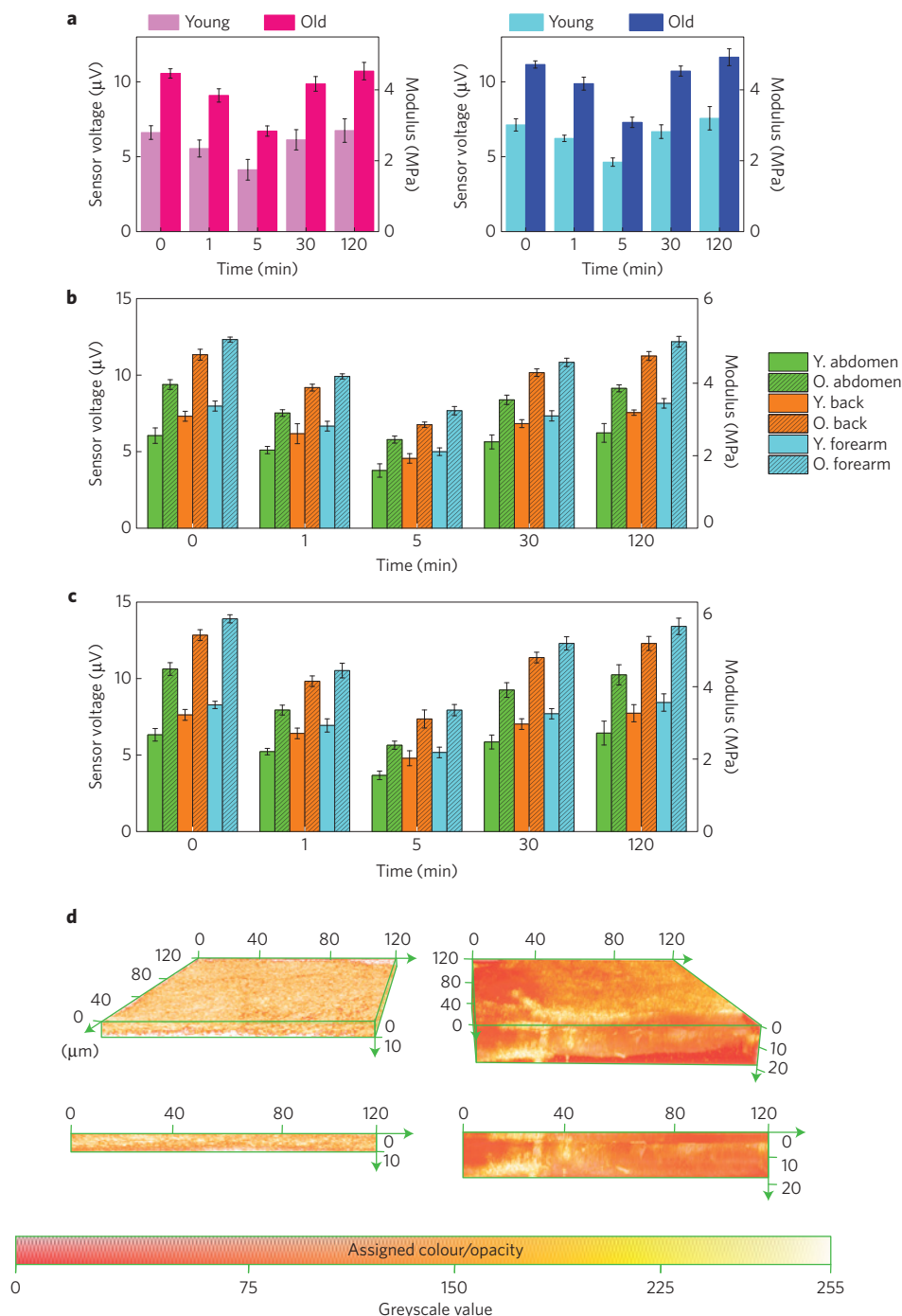
Figure 3 | Modulus measurements on *ex vivo* female and male skin samples as a function of time before and after application of a moisturizing lotion.
a, Sensor voltage and CMS modulus values at an actuation voltage and frequency of 5 V and 1 kHz, respectively, for *ex vivo* female (pink) and male (blue) abdominal skin for both young and old cases, at different times following application of 1% AMPS. **b,c**, Sensor voltage and CMS modulus values for *in vivo* female (**b**) and male (**c**) skin at different times following application of 1% AMPS. The measurements at 0 min correspond to unmodified skin (baseline), before application of AMPS. Measurements were performed on young (Y) and old (O) skin at three locations: abdomen, back and forearm. **d**, Visible laser confocal microscope images, in angled and cross-sectional views, of *ex vivo* young female abdominal skin before (left) and after (right) the application of 1% AMPS. In **a**–**c**, error bars correspond to calculated standard error deviation.

L'Oreal) applied on *ex vivo* abdominal skin samples from 35-year-old and 66-year-old females, and 33-year-old and 69-year-old males, appear in Fig. 3a (Supplementary Fig. 12 for age comparison, that is, 'young' = 33 and 35, 'old' = 66 and 69 years in age, Supplementary Fig. 13 for gender comparison). Supplementary Fig. 14 summarizes similar results for 3% glycerin and 3% urea. (In all cases, error bars correspond to calculated standard error.) Consistent with

expectation and previous reports[12,31], the modulus of skin generally increases with age, and is typically higher in males (3.01 MPa and 4.72 MPa for the 33- and 69-year-old cases, respectively) than females (2.79 MPa and 4.46 MPa for 35- and 66-year-old, cases, respectively). The magnitudes of the moduli lie between those measured using ultrasonic methods[30] or nanoindentation on *ex vivo* abdominal skin embedded in epoxy resin (Supplementary Fig. 15,
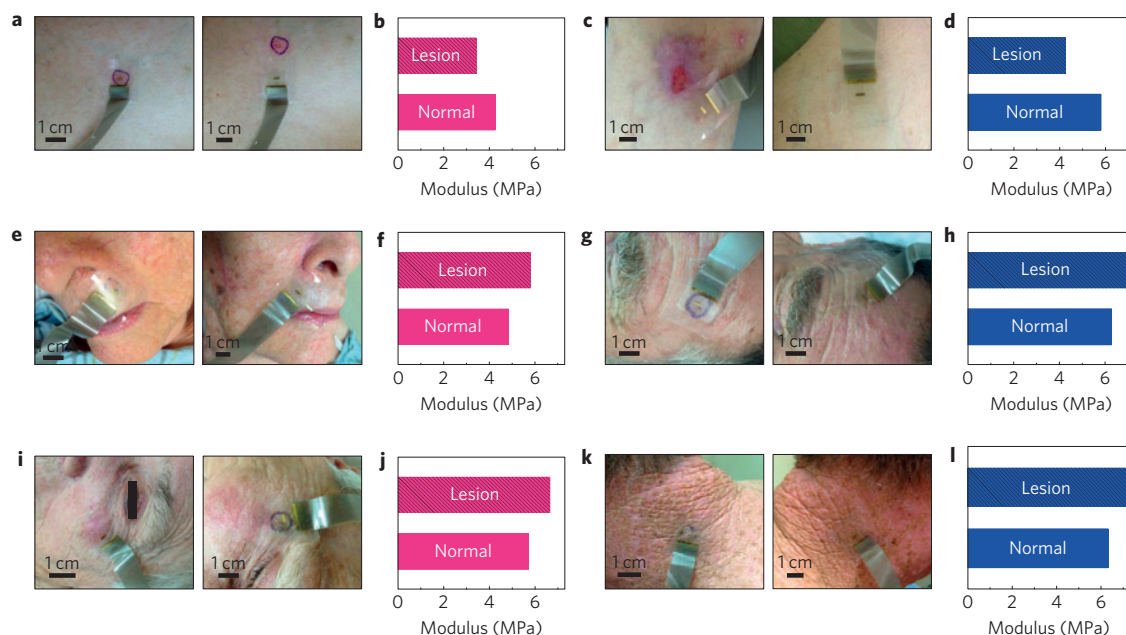
Figure 4 | CMS mapping of pathologies located on various body regions. a,c,e,g,i,k, Photographs of skin in regions with lesion (left) and of skin under normal conditions (right): breast (**a**), leg (**c**), near nose (**e**), forehead (**g**), near eye (**i**) and neck (**k**). **b,d,f,h,j,l**, CMS modulus values at an actuation voltage and frequency of 5 V and 1 kHz, respectively, for data collected in **a** (**b**), **c** (**d**), **e** (**f**), **g** (**h**), **i** (**j**), **k** (**l**).

Methods and Supplementary Table 1) and determined in the small-strain regimes with techniques based on tension[32,33], torsion[9,20] or suction[12,31]. Supplementary Table 2 summarizes similar trends observed by CMS and several other methods from the literature. In all cases, the percentage variations in moduli with gender are similar, with the exception of reports using suction, which suggest that female skin can exhibit a slightly higher modulus than male skin. Effects of age in both males and females are similar to those in other literature reports[34–36]. As skin ages, it becomes thinner, stiffer and less flexible[37].

Moisturizing agents tend to improve and/or restore the intrinsic properties of skin by modifying the mechanical and tribological behaviours. The AMPS solution offers the hydrating effects of glycerol and the plasticizing effects of urea, owing to strong interactions between the skin and the protein components of the solution[38]. The CMS data show that the plasticizing effect induces a temporary (∼5 min) reduction of Young's modulus, with a return to the initial state within ∼2 h, consistent with previous observations based on nanoindentation[38]. Although the modulus varies with position across the body, the overall trends with application of AMPS are similar, as summarized for measurements *in vivo* on skin in Fig. 3b,c. Visible laser confocal microscope images (Leica SP2) highlight the structural changes induced by moisturizers. As shown in Fig. 3d, application of 1% AMPS causes an increase in the thickness of the *ex vivo* abdominal skin (young female) by ∼80%, qualitatively consistent with related studies[39]. Skin from the old female, and the young and old male yield similar findings, as summarized in Supplementary Figs 16–18. The changes in fluorescence intensity correspond to decreases in the density of collagen due to swelling of the skin from uptake of the moisturizing agent, as illustrated in the histograms of intensity.

Moduli measured *in vivo* show similar trends with age, gender and application of moisturizing solutions. However, skin has the correct balance of extracellular and intracellular fluid, with little insensible fluid loss (evaporative loss) as a result of being intact and *in situ*, compared to *ex vivo* specimens. Consequently, *in vivo* tissues have lower moduli than those of well-maintained *ex vivo* samples. As an example of an important *in vivo* application, CMS

measurements can reveal localized changes in skin properties near lesion sites on a cohort of patients. This mode of operation has value in clinical examination, where skin tumours are typically noted to be stiffer than healthy tissue and can frequently be detected through physical palpations with detectable differences in mass, stiffness and viscoelasticity. Such differences manifest as a result of physical and molecular mechanisms underlying tumour progression[3], and can be used as biomarkers to assess the metastatic potential of cancer cells[40]. Results obtained from dermatologic malignancies in 30 patient volunteers indicate that skin lesions in breast and leg regions have lower moduli than in their healthy skin counterparts (Fig. 4a–d); however, skin lesions covering the nose and forehead regions have values higher than healthy skin counterparts (Fig. 4e–i). Such variability may be due to structural changes associated with frailty or skin thickness alterations as a result of ageing. Nevertheless, the computed modulus values and output voltages for measurements at different locations of the body (Supplementary Figs 19–22) provide a framework for mapping the stiffness of the skin. Comparisons between young–old, for female and male, appear in Supplementary Fig. 23. A summary of CMS performance on healthy and diseased skin is in Supplementary Figs 24–26. Because the neutral mechanical plane lies near the middle of the PZT layers, bending induces only minor changes in device operation (Supplementary Figs 11,27). Thus, curved contours of the body, such as the nose, finger and upper lip, may be readily wrapped for measurement (Supplementary Fig. 28).

The devices can also provide directional and spatial mapping of regional stiffness differences, via measurement modes that exploit the reversibility of the soft contact between CMS and skin. The results described here used a protractor (∼2 cm radius) printed on a transparent film (AF4300, 3M), with a rotatable segment (Fig. 5a). Aligning the modulus sensor to the window element and loosely connecting it with a thread enables calibrated rotations in clockwise and anticlockwise directions (Fig. 5b). Application of an adhesive film (3M Tegaderm Film) on top of the entire structure prevents movement during recording. Images associated with mapping the skin of a cancer patient (basal cell carcinoma) at the site of a lesion on both the forearm and the leg appear in Fig. 5c,e and Fig. 5d,f,
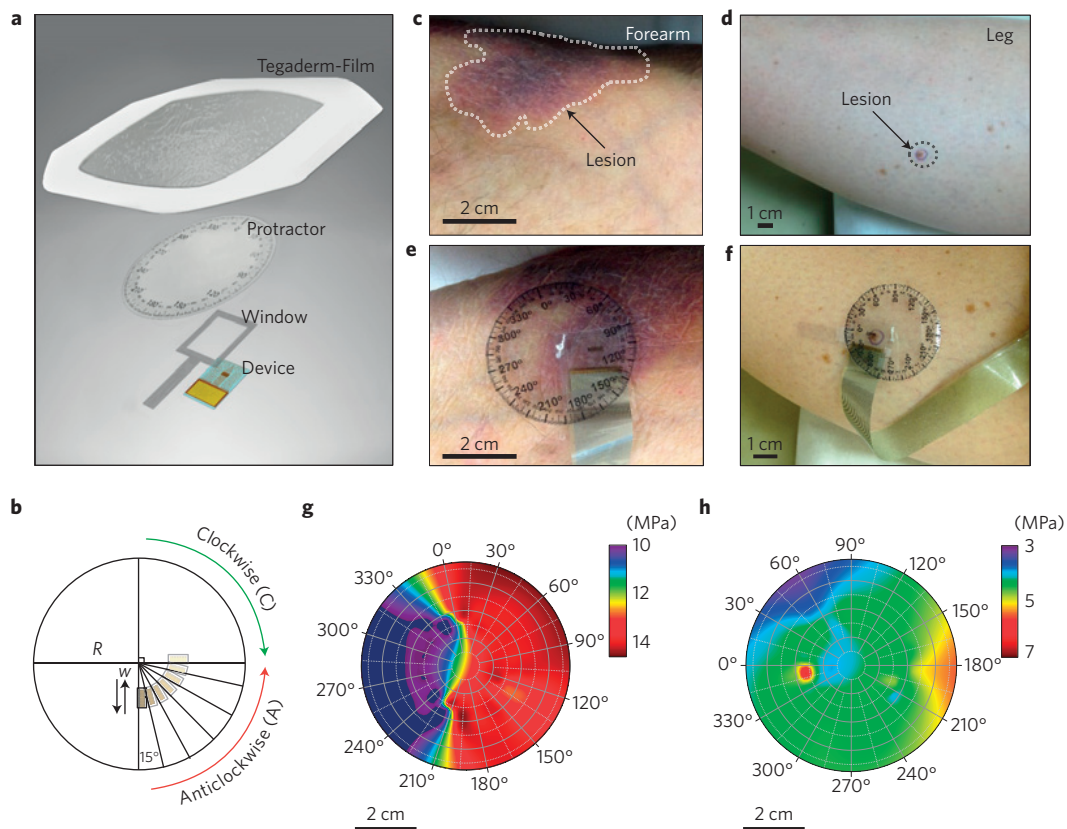
Figure 5 | Spatial mapping with a rotatable CMS system and *in vivo* evaluations on a cancer patient (basal cell carcinoma). a, Exploded-view schematic illustration of a system. **b**, Representative diagram of a device and its operation. *R* is the radius of the protractor and *w* is the distance between the centre of the protractor, and the edge of the first sensor in the array that defines the mapping area. **c,e**, Photograph of a forearm without (**c**) and with (**e**) a mounted device. **d,f**, Photographs of a lower leg without (**d**) and with (**f**) a mounted device. **g,h**, Data from experiments illustrated in **e** (**g**) and **f** (**h**).

respectively. The data in Fig. 5g,h correspond to measurements on the forearm and leg, respectively. Control measurements using a circular test substrate made using a PDMS substrate (∼33 kPa) with high-modulus (∼1,800 kPa) regions between 0° and 30° and between 90° and 120° are shown in Supplementary Fig. 29. Additional *in vivo* modulus mapping results from the forearm and hand are given in Supplementary Fig. 30.

The same CMS platforms can be applied to biological tissues other than the skin. As demonstrations, freshly explanted, unpreserved bovine organs—heart and lung—were tested. A previous report showed that PZT nanoribbons on silicone elastomer are capable of measuring mechanical deformations on a cow lung[41]. Measurements from the apex of the bovine heart, as well as the left (LV) and right (RV) ventricle, and lung appear in Fig. 6a–d. Stress–strain curves via DMA recorded from tissue samples ∼2 h after explantation (Fig. 6e) establish an estimate of the modulus values for these samples. Figure 6f compares these results with the CMS output voltages. The apex of the heart exhibits the highest modulus, as might be expected owing to the criss-crossing and confluence of multiple cardiac muscle and fibrous bands in this region[42]. The differences between moduli measured by DMA and CMS may arise from the absence of blood supply over the time required to prepare samples for DMA, which can lead to a relative dehydration state—that is, a decrease of both intra- and extracellular fluids—resulting in slightly stiffer mechanical properties. This time dependence can be tracked explicitly, by use of a CMS, as in Fig. 6g. A commercial moisture meter (MoistureMeterSC Compact, Delfin) establishes the change in the hydration level (H.L.) of the explanted LV contained in a scintillation vial with its cap opened half of a turn, at room temperature (native state), 1 h and 24 h after desiccation

in a 60 °C dry incubator. Figure 6h–j provides images collected at these different points in time. The findings suggest correlations between modulus, visible colour and dehydration state.

The concepts in materials and characterization methods introduced here create possibilities for rapid, 'on patient' measurements and spatial mapping of mechanical properties of the skin and other vital organs. For dermatologic investigation, the protocols of measurement are non-invasive and rapid, affording a high level of patient acceptance, as evidenced in this study by near-complete enrolment of approached volunteers (that is, 30/31, ∼97%) and by specific comments made by enrollees on procedure comfort and acceptability. *In vivo* clinical measurements, along with those on the various control samples and *ex vivo* organs, yield moduli that lie within an accepted range, with trends in terms of body positions and responses to moisturizing agents that are compatible with expectation, including local intradermal stiffness changes which correlate with intratissue pathology that may not be readily visible to the naked eye.

Future embodiments might incorporate high-density, further-miniaturized arrays of actuators/sensors to increase the sensitivity of focal stiffness resolution and realize capabilities in rapidly accessible spatial resolution, which could easily exceed those achievable by human touch on physical exam. The spatial resolution is important to examine microscale disorders such as fibrous histiocytoma, fibroepithelial polyp, and basal ganglia carcinoma in office- or hospital-based dermatologic screening and examination. Similar systems may be fashioned to measure mechanical property changes over time, for clinical monitoring of a wide range of conditions, where variations are anticipated due either to time-dependent alterations in pathophysiology or a response to therapy. The ability to deploy
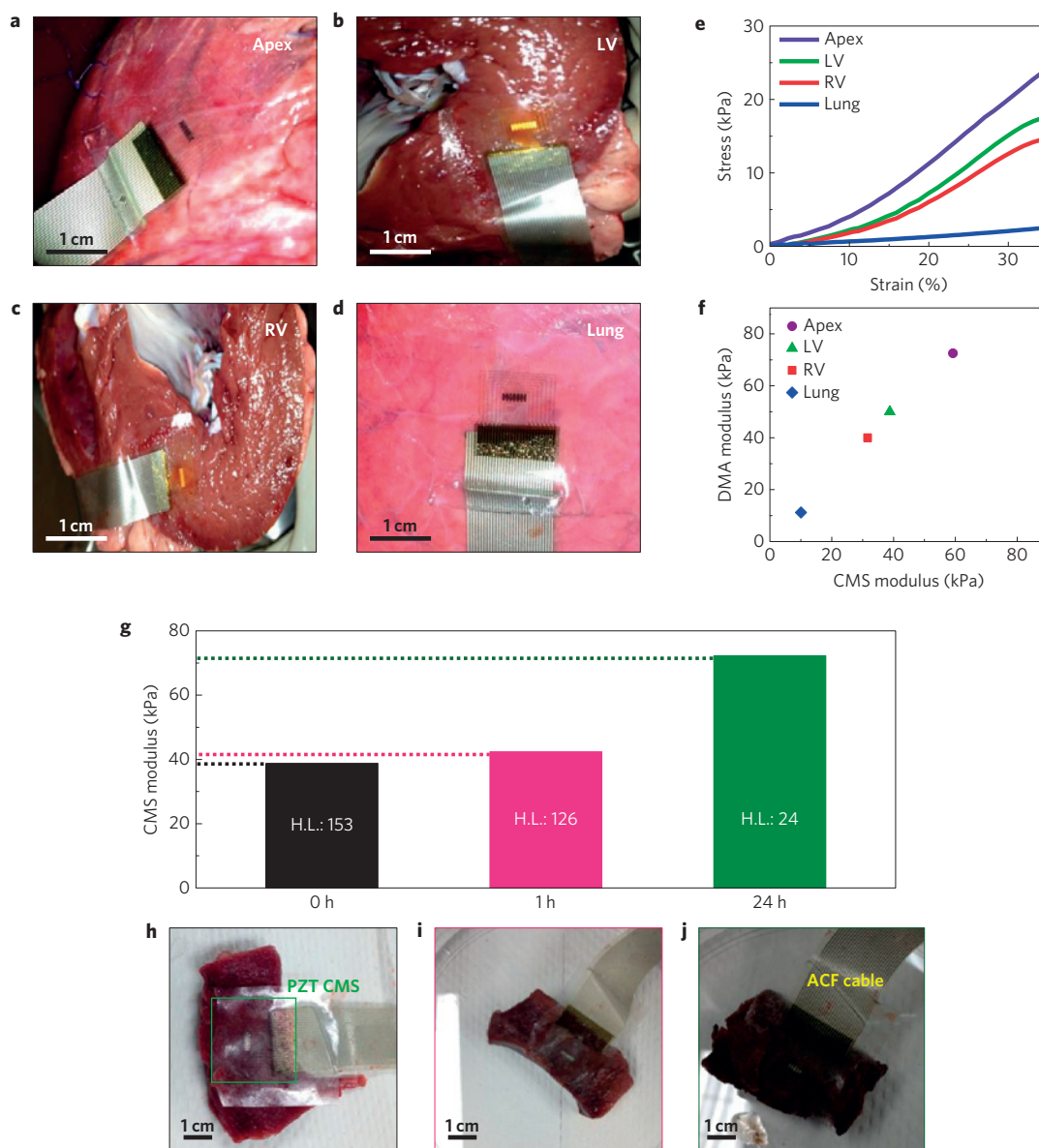
Figure 6 | Ex vivo CMS measurements on bovine organs. a–d, Photographs of a device placed on: heart apex (**a**), left ventricle (LV) (**b**), right ventricle (RV; **c**) and lung (**d**). **e,** Stress–strain curves on tissue samples. **f,** Modulus values extracted from the data in **e** and from CMS measurements (actuation voltage and frequency of 5 V and 1 kHz, respectively), as a function of sensor voltage. **g,** Variation in modulus of a piece of explanted LV as a function of time. **h–j,** Photographs of a device placed on a piece of explanted LV kept at room temperature for 0 h (**h**), 60 °C for 1 h (**i**), and 60 °C for 24 h (**j**). ACF, anisotropic conductive film.

this technology to internal organs of the body through catheters, trochars or endoscopes provides additional areas of opportunity.

Methods

Methods and any associated references are available in the online version of the paper.

References

1. Elias, P. M. Stratum corneum defensive functions: An integrated view. *J. Gen. Intern. Med.* **20,** 183–200 (2005).
2. Charkoudian, N. Skin blood flow in adult human thermoregulation: How it works, when it does not, and why. *Mayo Clin. Proc.* **78,** 603–612 (2003).
3. Paszek, M. J. *et al.* Tensional homeostasis and the malignant phenotype. *Cancer Cell* **8,** 241–254 (2005).
4. Friberg, S. E. Micelles, microemulsions, liquid crystals, and the structure of stratum corneum lipids. *J. Soc. Cosmet. Chem.* **41,** 155–171 (1990).
5. Reiger, M. M. & Deem, D. Skin moisturizers. II. The efects of cosmetic ingredients on human SC. *J. Soc. Cosmet. Chem.* **25,** 253–262 (1974).
6. Magnenat-Thalmann, N. *et al.* A computational skin model: Fold and wrinkle formation. *IEEE Trans. Inf. Technol. Biomed.* **6,** 317–323 (2002).
7. Batisse, D., Bazin, R. & Baldeweck, T. Influence of age on the wrinkling capacities of skin. *Skin Res. Technol.* **8,** 148–154 (2002).
8. Alexander, H. & Cook, T. Variations with age in the mechanical properties of human skin *in vivo. J. Tissue Viabil.* **16,** 6–11 (2006).
9. Leveque, J. L., Rigal, J. de, Agache, P. G. & Monneur, C. Influence of ageing on the *in vivo* extensibility of human skin at a low stress. *Arch. Dermatol. Res.* **269,** 127–135 (1980).
10. Li, C., Guan, G., Reif, R., Huang, Z. & Wang, R. K. Determining elastic properties of skin by measuring surface waves from an impulse mechanical stimulus using phase-sensitive optical coherence tomography. *J. R. Soc. Interface* **9,** 831–841 (2012).
11. Hendriks, F. M. *Mechanical Behaviour of Human Epidermal and Dermal Layers In Vivo* (Technische Universiteit Eindhoven, 2005).

12. Diridollou, S. *et al.* Sex and site dependent variations in thickness and mechanical properties of human skin *in vivo. Int. J. Cosmet. Sci.* **22,** 421–435 (2000).

13. Kashibuchi, N., Hirai, Y., O'Goshi, K. & Tagami, H. Three-dimensional analyses of individual corneocytes with atomic force microscope: Morphological changes related to age, location and to the pathologic skin conditions. *Skin Res. Technol.* **8,** 203–211 (2002).

14. Lulevich, V., Zink, T., Chen, H-Y., Liu, F-T. & Liu, G. Cell mechanics using atomic force microscopy-based single-cell compression. *Langmuir* **22,** 8151–8155 (2006).

15. Elias, P. M. Structure and function of the stratum corneum permeability barrier. *Drug Dev. Res.* **13,** 97–105 (1988).

16. Lumpkin, E. A. & Caterina, M. J. Mechanisms of sensory transduction in the skin. *Nature* **445,** 858–865 (2007).

17. Bommannan, D., Potts, R. O. & Guy, R. H. Examination of stratum corneum barrier function *in vivo* by infrared spectroscopy. *J. Invest. Dermatol.* **95,** 403–408 (1990).

18. Diridollou, S. *et al. In vivo* model of the mechanical properties of the human skin under suction. *Skin Res. Technol.* **6,** 214–221 (2000).

19. Hendriks, F. M. *et al.* A numerical-experimental method to characterize the non-linear mechanical behaviour of human skin. *Skin Res. Technol.* **9,** 274–283 (2003).

20. Sanders, R. Torsional elasticity of human skin *in vivo. Pflüg. Arch.* **342,** 255–260 (1973).

21. Berardesca, E., de Rigal, J., Leveque, J. L. & Maibach, H. I. *In vivo* biophysical characterization of skin physiological differences in races. *Dermatology* **182,** 89–93 (1991).

22. Sugihara, T., Ohura, T., Homma, K. & Igawa, H. H. The extensibility in human skin: Variation according to age and site. *Br. J. Plast. Surg.* **44,** 418–422 (1991).

23. Fischer-Cripps, A. C. Critical review of analysis and interpretation of nanoindentation test data. *Surf. Coat. Technol.* **200,** 4153–4165 (2006).

24. Gennisson, J. L. *et al.* Assessment of elastic parameters of human skin using dynamic elastography. *IEEE Trans. Ultrason. Ferroelectr. Freq. Control* **51,** 980–989 (2004).

25. Dagdeviren, C. *et al.* Conformable amplified lead zirconate titanate sensors with enhanced piezoelectric response for cutaneous pressure monitoring. *Nature Commun.* **5,** 4496 (2014).

26. Christensen, R. *Theory of Viscoelasticity: An Introduction* (Elsevier, 1982).

27. Then, C., Vogl, T. J. & Silber, G. Method for characterizing viscoelasticity of human gluteal tissue. *J. Biomech.* **45,** 1252–1258 (2012).

28. Cui, T., Lin, C-W., Chien, C. H., Chao, Y. J. & Van Zee, J. W. Service life estimation of liquid silicone rubber seals in polymer electrolyte membrane fuel cell environment. *J. Power Sources* **196,** 1216–1221 (2011).

29. Cheng, H. *et al.* A viscoelastic model for the rate effect in transfer printing. *J. Appl. Mech.* **80,** 041019–041019 (2013).

30. Lin, I-K. *et al.* Viscoelastic mechanical behavior of soft microcantilever-based force sensors. *Appl. Phys. Lett.* **93,** 251907 (2008).

31. Barel, A. O., Lambrecht, R. & Clarys, P. Mechanical function of the skin: State of the art. *Curr. Probl. Dermatol.* **26,** 69–83 (1998).

32. Silver, F. H., Seehra, G. P., Freeman, J. W. & DeVore, D. Viscoelastic properties of young and old human dermis: A proposed molecular mechanism for elastic energy storage in collagen and elastin. *J. Appl. Polym. Sci.* **86,** 1978–1985 (2002).

33. Stark, H. L. Directional variations in the extensibility of human skin. *Br. J. Plast. Surg.* **30,** 105–114 (1977).

34. Ryu, H. S., Joo, Y. H., Kim, S. O., Park, K. C. & Youn, S. W. Influence of age and regional differences on skin elasticity as measured by the Cutometer. *Skin Res. Technol.* **14,** 354–358 (2008).

35. Escoffier, C. *et al.* Age-related mechanical properties of human skin: An *in vivo* study. *J. Invest. Dermatol.* **93,** 353–357 (1989).

36. Grahame, R. & Holt, P. J. L. The influence of ageing on the *in vivo* elasticity of human skin. *Gerontology* **15,** 121–139 (1969).

37. Pawlaczyk, M., Lelonkiewicz, M. & Wieczorowski, M. Age-dependent biomechanical properties of the skin. *Postepy Dermatol. Alergol.* **30,** 302–306 (2013).

38. Luengo & Galliano A. *Scanning Probe Microscopy for Industrial Applications: Nanomechanical Characterization* Vol. 12 (John Wiley, 2013).

39. Richter, T., Müller, J. H., Schwarz, U. D., Wepf, R. & Wiesendanger, R. Investigation of the swelling of human skin cells in liquid media by tapping mode scanning force microscopy. *Appl. Phys. A* **72,** S125–S128 (2001).

40. Xu, W. *et al.* Cell stiffness is a biomarker of the metastatic potential of ovarian cancer cells. *PLoS ONE* **7,** e46609 (2012).

41. Nguyen, T. D. *et al.* Piezoelectric nanoribbons for monitoring cellular deformations. *Nature Nanotech.* **7,** 587–593 (2012).

42. Fernandez-Teran, M. A. & Hurle, J. M. Myocardial fiber architecture of the human heart ventricles. *Anat. Rec.* **204,** 137–147 (1982).

Author contributions

C.D. and J.A.R. designed the research; C.D., P.J., G.B., K.U., O.G., P.L.T., J.R.C., M.M., M.J.S. and J.A.R. performed the research; C.D., Y.Shi., R.C.W., Y.H. and J.A.R. contributed new reagents/analytic tools; Y.Su assisted in designing the device structure; C.D., Y.Shi, P.J., G.B., P.L.T., J.R.C., A.S.T., M.J.S., Y.H. and J.A.R. analysed data; and C.D., Y.Shi, R.G., G.B., M.J.S., Y.H. and J.A.R. wrote the paper.

Additional information

Supplementary information is available in the online version of the paper. Reprints and permissions information is available online at www.nature.com/reprints. Correspondence and requests for materials should be addressed to J.A.R.

Competing financial interests

The authors declare no competing financial interests.

Methods

Fabrication of PZT actuator and sensor arrays. Fabrication of the actuator and sensor arrays began with formation of a 500-nm-thick film of PZT (INOSTEK) by sol–gel techniques on an oxidized silicon wafer[25,43] (Supplementary Fig. 1). Selection of the PZT thickness balanced considerations in bendability, where thinner is better, and in sensor voltage output, where thicker is better. A 500-nm-thick PZT layer represents a good choice. The spaces between the sensors and actuators facilitate access of concentrated hydrofluoric acid for undercut etching of the PZT elements. The array structure provides modulus values at specific locations under actuator and sensor pairs. Serpentine conducting traces provide a stretchable device platform. The actuator layers included a $260 \times 1,300\,\mu m^2$ bottom electrode (Pt/Ti; 300 nm/20 nm), a $200 \times 1,000\,\mu m^2$ PZT layer and $140 \times 940\,\mu m^2$ top electrode (Au/Cr; 200 nm/10 nm). The sensor layers included a $160 \times 660\,\mu m^2$ bottom electrode (Pt/Ti; 300 nm/20 nm), $100 \times 500\,\mu m^2$ PZT layer and $60 \times 460\,\mu m^2$ top electrode (Au/Cr; 200 nm/10 nm). Photolithography with standard photoresist (PR, AZ5214E) defined the top Au/Cr electrode structure. The Au and Cr layers were etched with gold etchant (TFA, Transene Company) and CR-7 chrome etchant (OM Group), respectively. Wet chemical etching with a solution of HNO_3:BHF:H_2O (nitric acid:buffered hydrofluoric acid:DI water ratio of 4.51:4.55:90.95) through a hard-baked (80 °C for 5 min, 110 °C for 30 min and 80 °C for 5 min) mask of photoresist (PR; AZ4620, Clariant) defined a corresponding pattern in the PZT (Supplementary Fig. 2b). Etching with a solution of HCl:HNO_3:H_2O (DI water) = 3:1:4 at 95 °C and a similar PR mask (Supplementary Fig. 2e) patterned the bottom Pt/Ti electrode structure. Another hard-baked PR mask protected the PZT during elimination of the underlying SiO_2 layer with diluted hydrofluoric acid (H_2O: 49% HF = 1:3 by volume). Immersion in an acetone bath at room temperature for ∼3 h washed away the PR (Supplementary Fig. 1b). Application and removal of a piece of thermal tape (REVALPHA, Nitto Denko) retrieved the PZT devices from the silicon wafer (Supplementary Fig. 1c). A separate wafer coated with a 50-nm-thick layer of poly(methyl methacrylate) (PMMA 495 A2, 3,000 rpm (Headway Research, PWM32) for 30 s, baked on a hotplate at 180 °C for 2 min) and a 1.2-μm-thick layer of PI (from poly(pyromellitic dianhydride-co-4,40-oxydianiline) amic acid solution; 4,000 rpm (g-value=715) for 30 s, pre-cured on a hotplate at 150 °C for 1 min) served as a temporary substrate. Heating at 250 °C for 1 min partially cured the PI to provide a tacky surface. Transfer (Supplementary Fig. 1d) occurred by laminating the tape with PZT devices onto this substrate, heating to ∼150 °C (on hot plate) and then removing the tape. Baking at 250 °C for 1 h in a vacuum oven at 10 mtorr completed the curing of the PI. A uniform 1.2-μm-thick layer of PI spin cast and cured (250 °C for 1 h) on the PZT devices protected their top surfaces. Openings through the PI, formed by reactive ion etching (March RIE) through a pattern of PR, provided access to the metal electrode contacts (Supplementary Fig. 2i,j). Evaporation and photolithographic patterning of Au/Cr (200 nm/10 nm) defined metal interconnects. Another patterned 1.2-μm-thick PI layer formed an encapsulation layer that left the PMMA layer exposed for removal by immersion in acetone at 100 °C (Supplementary Fig. 1e). Thermal tape again served as a vehicle for retrieving the devices (Supplementary Fig. 1f). A layer of Ti/SiO_2 (4 nm/40 nm) evaporated onto the exposed backside of the devices provided an adhesive layer for bonding onto a 20-μm-thick film of silicone (Ecoflex 00-30, Smooth-On; weight ratio of 1A:1B) on a substrate of poly(vinylalcohol) (PVA; A-30031, Best Triumph Industrial) temporarily held to a glass slide by a layer of polydimethylsiloxane (PDMS, Sylgard 184). Transfer from the thermal tape used procedures similar to those described previously (Supplementary Fig. 1g). The mounting process involved placing the PZT sensor and actuator arrays against the skin and then gently washing away the PVA with water (Fig. 1e,f). As reported in refs 25,43, PZT devices with related construction but configured for other purposes remain stable across a range of temperatures and humidities. The air or moisture permeability through the PI (poly(pyromellitic dianhydride-co-4,40-oxydianiline)) is strictly constrained by strong interchain attraction forces and a high degree of molecular packing, as described in ref. 44. This type of encapsulation prevents any direct contact of PZT with adjacent biological tissues. The CMS device encapsulated with PI is highly water resistant, functioning well in moist environments, and providing comparable modulus values to those measured by DMA.

Directional modulus mapping. A sensor (Supplementary Fig. 31c) aligned to a protractor with a 2 cm radius (R) printed on a transparent film (AF4300, 3M) and mounted in a rotatable fashion (Supplementary Fig. 31) served as a tool for directional modulus mapping. The CMS was rotated clockwise (C) or anticlockwise (A) with an angle increment of 15°. The distance, w, between the centre of the protractor and the edge of the first sensor in the array defines the mapping area. A 3M Tegaderm Film laminated on the top surface prevented motion during measurement (Supplementary Fig. 31d–h).

Confocal microscopy. Imaging through the depth of skin involved a Leica SP2 Visible Laser Confocal Microscope (oil immersion, numerical aperture 1.40, lateral optical resolution 240 nm) with a ×63 objective and 633 nm laser illumination. Glass slides (170 μm thick) served as supports for the skin samples.

Three-dimensional (3D) reconstruction used standard software tools (Amira Software 5.0.2). The detection bandwidth (±10 nm) and gain were fixed for all samples, to facilitate comparisons. Human skin has autofluorescence due to collagen structure, thus no fluorophore was needed.

Poling the PZT. Poling involved application of an electric field (∼100 kV cm^{-1}) at 150 °C for 2 h (ref. 45) to PZT thin films between the bottom and top contacts of Ti/Pt (20 nm/300 nm) and Cr/Au (10 nm/200 nm), respectively.

Device operation. A recording system consisting of a lock-in amplifier (SR830, Standard Research Systems), a multiplexer (FixYourBoard.com, U802) and a laptop computer enabled collection of data from the sensors and application of driving voltages to the actuators. A flexible ribbon cable (HST-9805-210, Elform) connected arrays of six sensors to a multiplexer, for sequential interrogation (Supplementary Fig. 32).

Preparation of artificial skin samples. Artificial skin samples consisted of a mixture of commercially available materials: Dragon Skin (Dragon Skin 30, Smooth-On), Silc Pig (Silc Pig, Flesh tone silicone pigment, Smooth-On) and Ecoflex (Eco Flex 30, Smooth-On). The Dragon Skin (1:1 weight ratio of part A and part B) was mixed with Silc Pig (3% by weight; Supplementary Fig. 33) and then placed on the forearm of a male volunteer (Supplementary Fig. 33a), where it was allowed to cure under ambient conditions for ∼1 h (Supplementary Fig. 33c–e). Removing the material (Supplementary Fig. 33f,g) and placing it in a plastic Petri dish (Supplementary Fig. 33h) with the textured side up allowed it to be used as a mould. Ecoflex (1:1 weight ratio of A:B) was then mixed with Silc Pig (3% by weight), placed in a vacuum chamber for 0.5 h, and then poured on the top of the Dragon Skin sample (Supplementary Fig. 33i). Peeling the cured material away after curing for 12 h at room temperature yielded samples of artificial skin (Supplementary Fig. 33j).

Scanning electron microscopy and image preparation. Scanning electron microscopy (HITACHI S-4800 SEM) provided images of devices mounted on artificial skin. The colourization process used the colour burn function in Adobe Photoshop CS6 (Fig. 1f,g and Supplementary Fig. 4), with the following RGB values for the different layers: gold (218, 165, 32), PZT (57, 206, 72), PI (243, 111, 39), skin (190, 142, 122).

Nanoindentation. Skin embedded in epoxy resin was cut in 100-nm-thick sections using a Leica UC-6 ultra-microtome, leaving a polished surface for indentation testing. Testing occurred at 45% ± 5% humidity and 20 °C, with a TriboScope nanoindenter (Hysitron) mounted on a multimode atomic force microscope (AFM) controlled by NanoScope IIIa electronics (Veeco). The tip radius determined by examination with an SEM agreed (within 90%) with this calibrated value. A force with a trapezoidal time profile applied to the skin surface generated a load–displacement curve that allowed quantification of elastic modulus and hardness[46]. Consecutive measurements were separated by 2 μm to minimize the influence of prior indentations.

Dynamic mechanical analysis. Dynamic mechanical analysis (Q800 DMA, TA Instruments) allowed measurement of quasi-static stress–strain curves of a set of substrates of polydimethylsiloxane (PDMS, Sylgard 184, Dow Corning) formed using different conditions to yield a range of Young's moduli (Supplementary Fig. 8). Each PDMS substrates had dimensions of $3.5 \times 6.0 \times 2.0\,mm^3$ (width × length × thickness). The measurements used the DMA film tension clamp in ambient conditions, with a strain rate of 10% min^{-1} to a maximum value of 100%.

***In vitro* biocompatibility assessment.** Experiments involved human epithelial keratinocytes (HEK) purchased from Life Technologies (HEKa), cultured in T-75 tissue culture flasks with Medium 154 medium (Life Technologies) supplemented with human keratinocyte growth supplement (Life Technologies) and 1% Pen/Strep-amphotericin B (Lonza). The complete culture medium was stored at 4 °C for use within four weeks from the time of preparation. HEK cells were sub-cultivated and cultured in an incubator for all studies (37 °C, 5% CO_2, and 95% relative humidity). Cell used for seeding on the sensor surface were passage 2–5 before seeding on sensor surface. The biocompatibility studies involved seeding HEK (∼20,000) onto strips of sensor devices (1 cm^2 pieces, sterilized under ultraviolet light for 30 min on each side) and incubating them for 1 or 3 days, as outlined above, with medium change every 48 h. On day 1, cells were stained using an actin cytoskeleton/focal adhesion staining kit (Millipore). Cells were fixed with 4% paraformaldehyde for 15 min, washed, then permeabilized with 0.05% Triton-X for 5 min, washed, and then blocked with 1% protein standard (fractionated bovine serum albumin) in PBS at pH 7.4. Cells were then incubated with tetramethyl rhodamine isothiocyanate (TRITC) conjugated phalloidin for 1 h to selectively label F-actin. After rinsing, cells were then mounted in a vector shield with DAPI (Sigma-Aldrich) and imaged using a Nikon C1Si Laser Scanning Confocal Fluorescence Microscope (Supplementary Fig. 3b). Scanning electron microscopy

(SEM, FEI Inspect S, Thermo) revealed the extent of adherence of cells to the sensor substrates. For this purpose, following 24 h of culture, HEK were fixed in 5% glutaraldehyde in PBS, pH 7.4, subjected to a graded series of water and ethanol (100% fixator → 3:1 → 1:1 → 1:3 → 100% distilled water → 3:1 → 1:1 → 1:3 → 100% ethanol) at 5 min for each step and then critical point dried (Polaron model 3100, Energy Beam Sciences). Specimens were then mounted on aluminium stubs, sputter-coated with gold (5–8 nm, Hummer Sputtering System, Anatech) and imaged at voltages between 5 and 15 kV with an aperture of 3. The viability, proliferation and cytotoxicity of HEK were determined by a two-colour fluorescence LIVE/DEAD viability (Invitrogen) assay, lactate dehydrogenase (LDH) assay (Thermo), and MTT assay. For the LIVE/DEAD assay, HEK grown on sensor strips for one day were prepared and stained according to standard protocols (Sigma-Aldrich). Briefly, culture dish wells were aspirated, washed and a working solution (consisting of 5 ml 1 × PBS, 10 µl of 2 mM EthD-1 and 2.5 µl of 4 mM calcein AM) was then added to cover each of the samples. Submerged samples were incubated for 30 min at 37 °C. The working solution was then removed, and the samples were rinsed once with 1 × PBS, then mounted in Fluoroshield and immediately imaged by fluorescence microscopy (Nikon C1Si). The LDH cytotoxicity assay involved mixing 50 µl medium from HEK grown for 1 and 3 days with a 50 µl reaction mixture (prepared according to the manufacture's recipe) in a 96-well plate and incubating for 30 min at room temperature. A stop solution (50 µl) was then added and the optical absorbance was immediately measured at 490 and 680 nm. The mean percentages of healthy cells were reported with standard errors of the mean. For the MTT assay, 100 µl of a 5 mg ml^{-1} solution of thiazolyl blue tetrazolium bromide (Alfa Aesar) was added to cells in a 24-well plate. After 3.5 h of incubation at 37 °C, 5% CO$_2$ and 95% relative humidity, the well contents were removed and 300 µl of dimethyl sulphoxide was added to each well. The well plate was rocked slowly for 10 min and the contents of each well were then transferred to a 96-well plate, where the absorbance was determined at 590 and 620 nm. True absorbance was calculated by subtracting the reading at 590 nm from that at 620 nm. As a positive control, 5% sodium dodecyl sulphate (SDS) was added to cells seeded in control tissue culture plate wells 1 h before removal of the thiazolyl blue tetrazolium bromide and the cell media from some of the wells. All readings were compared against cells seeded in 24-well plates on the tissue culture surface. Results correspond to the percentage absorbance compared to the values of the tissue culture plates. To demonstrate feasibility for external placement, temporary use, and to ensure that there was no alteration in the functional groups on the surfaces of the sensors after culturing with cells and submersion in cell media for seven days, attenuated total reflectance-Fourier transform infrared spectroscopy (ATR-FTIR; Thermo Nicolet 370-FT-IR, Thermo Scientific) was used to obtain the infrared transmittance before and after the sensors had been cultured with HEK. The spectrum was collected with 32 data points (Supplementary Fig. 3e).

Ex vivo modulus (material property) assessment. Freshly excised bovine hearts and lungs ($n = 3$) were used for determination of the regional material properties using the piezoconstructs. The heart was selected as a prototypic solid organ, as differing regions have clear material property differences based on differing histoarchitecture, variable thickness and perfusion. Further, the curvilinearity and complex geometry served as a stringent test for the efficacy of the constructs. Constructs were laminated on the LV, RV, apex sites of the hearts and the surface of lung. The intimate integration between curly, soft tissue and conformal constructs on silicone substrates was driven by van der Waals forces alone, without application of an adhesive layer, thereby leading to a conformal, precise, completely non-invasive measurement (Supplementary Fig. 32). All animal studies were approved by the Institutional Animal Care and Use Committee at the University of Arizona.

In vivo modulus (material property) assessment. Forty human volunteers were used for the described studies. Volunteers were at rest during the measurements, which each lasted ∼10 s. Ten volunteers (five female, five male) were recruited for studies on normal skin, with all of these free of visible skin lesions. Thirty patients with a range of dermatologic conditions (15 female, 15 male) including: fibrous histiocytoma, lichenoid keratosis, seborrhoeic keratosis, actinic keratosis, squamous cell carcinoma, basal cell carcinoma, compound nevus, haemangioma, fibroepithelial polyp, superficial perivascular and interface lymphocytic dermatitis, erosive dermatitis, severely atypical compound melanocytic proliferation, and bullous pemphigoid were studied, as seen in Supplementary Figs 24–27. All subjects (normal and patients) were volunteers for this study, were informed of risks and benefits, and provided informed consent.

Statistical analysis. Statistical tests for biocompatibility assessment were performed using Microsoft Excel v2010. Means with standard error of the mean were reported. Single comparison t-tests were used in two-population comparisons. Differences were considered significant if $p < 0.05$.

References

43. Dagdeviren, C. *et al.* Conformal piezoelectric energy harvesting and storage from motions of the heart, lung, and diaphragm. *Proc. Natl Acad. Sci. USA* **111,** 1927–1932 (2014).
44. Calle, M., Lozano, A. E., de Abajo, J., de la Campa, J. G. & Álvarez, C. Design of gas separation membranes derived of rigid aromatic polyimides. 1. Polymers from diamines containing di-tert-butyl side groups. *J. Membr. Sci.* **365,** 145–153 (2010).
45. Dagdeviren, C. *et al.* Transient, biocompatible electronics and energy harvesters based on ZnO. *Small* **9,** 3398–3404 (2013).
46. Balooch, G. *et al.* TGF-β regulates the mechanical properties and composition of bone matrix. *Proc. Natl Acad. Sci. USA* **102,** 18813–18818 (2005).

Conformal piezoelectric systems for clinical and experimental characterization of soft tissue biomechanics

Canan Dagdeviren[a,b], Yan Shi[c,d], Pauline Joe[a], Roozbeh Ghaffari[e], Guive Balooch[f], Karan Usgaonkar[a], Onur Gur[g], Phat L. Tran[h], Jessi R. Crosby[h], Marcin Meyer[i], Yewang Su[d,j], R. Chad Webb[a], Andrew S. Tedesco[k], Marvin J. Slepian[h,l], Yonggang Huang[d], John A. Rogers[a,g,m]

[a]*Department of Materials Science and Engineering, Beckman Institute for Advanced Science and Technology, and Frederick Seitz Materials Research Laboratory, University of Illinois at Urbana-Champaign, Urbana, IL 61801*
[b]*The David H. Koch Institute for Integrative Cancer Research, Massachusetts Institute of Technology, Cambridge MA 02139*
[c]*State Key Laboratory of Mechanics and Control of Mechanical Structures, Nanjing University of Aeronautics & Astronautics, Nanjing 210016, China*
[d]*Department of Civil and Environmental Engineering, Department of Mechanical Engineering, Center for Engineering and Health and Skin Disease Research Center, Northwestern University, Evanston, IL 60208.*
[e]*MC10 Inc., Cambridge, MA 02140*
[f]*L'Oreal R&I Incubator, Department of Research and Innovation, Clark, NJ 07066*
[g]*Department of Electrical and Computer Engineering, University of Illinois at Urbana-Champaign, Urbana, IL 61801*
[h]*Department of Medicine & Sarver Heart Center, The University of Arizona, Tucson, AZ 85724*
[i]*Institute for Materials Science and Max Bergmann Center of Biomaterials, TU Dresden, 01062 Dresden, Germany*
[j]*Center for Mechanics and Materials, Tsinghua University, Beijing 100084, China*
[k]*Academy Dermatologist Group, Ltd, Tucson, AZ 85710*
[l]*Department of BioMedical Engineering, The University of Arizona, Tucson, AZ 85724*
[m]*Department of Chemistry and Department of Mechanical Science and Engineering, University of Illinois at Urbana-Champaign, Urbana, IL 61801*

To whom correspondence should be addressed. E-mail: jrogers@illinois.edu

Supplementary Note 1: Neutral Mechanical Plane and Bending Stiffness

For the multilayer structure with n layers subjected to pure bending, the cross-section remains planar after bending in the classical beam theory. The neutral mechanical plane, located by the distance $y_{neutral}$ from the bottom surface of the multilayer structure (Supplementary Fig. S11) is given by[1]

$$y_{neutral} = \frac{\sum_{k=1}^{n} \bar{E}_k h_k \left(\sum_{j=1}^{k} h_j - \frac{h_k}{2} \right)}{\sum_{k=1}^{n} \bar{E}_k h_k}, \tag{S1}$$

where $\bar{E}_k = E_k / (1 - \nu_k^2)$ and h_k are the plane-strain modulus and thickness of the kth layer, respectively, with $k=1$ for the bottom layer. The bending stiffness of the structure is given by

$$\overline{EI} = \sum_{k=1}^{n} \bar{E}_k h_k \left[\left(y_{neutral} - \sum_{j=1}^{k} h_j \right)^2 + \left(y_{neutral} - \sum_{j=1}^{k} h_j \right) h_k + \frac{1}{3} h_k^2 \right]. \tag{S2}$$

For the structure in Supplementary Fig. S11, the Young's modulus of elastomer substrate (silicone, 60 kPa) is much smaller than those of the other layers of the device by 5 to 7 orders of magnitude. The elastomer layer has a negligible effect on the effective bending stiffness and the neutral mechanical plane of the cross section. For the thickness given in Supplementary Fig. S11 and the plane-strain modulus of PI ($\bar{E}_1 = \bar{E}_7 = 2.83 GPa$), Au ($\bar{E}_2 = 96.7 GPa$), Cr ($\bar{E}_3 = 292 GPa$), PZT ($\bar{E}_4 = 42.1 GPa$), Pt ($\bar{E}_5 = 196 GPa$) and Ti ($\bar{E}_6 = 124 GPa$), the neutral mechanical plane is at $y_{neutral} = 2.99 \mu m$, which is located around the middle of the PZT layer. The corresponding bending stiffness is

$\overline{EI} = 4.55 \times 10^{-8}$ Nm. The location of the neutral mechanical plane layout with respect to the PZT is important. For the bending radius varying from 22 mm to 150 mm (22 mm, 58 mm, 150 mm) in Supplementary Fig. S27, the corresponding strain in PZT layer is less than 0.002%, which is negligible as compared to the strain field induced by voltage. The results have been validated by the output voltage of the sensors (Supplementary Fig. S27). Therefore, the sensor voltages are almost the same when laminated on the flat and curvature surfaces.

Supplementary Note 2: Piezoelectric Analysis

The constitutive model of piezoelectric material gives

$$
\begin{Bmatrix} \sigma_{11} \\ \sigma_{22} \\ \sigma_{33} \\ \sigma_{23} \\ \sigma_{31} \\ \sigma_{12} \end{Bmatrix} =
\begin{bmatrix} c_{11} & c_{12} & c_{13} & 0 & 0 & 0 \\ c_{12} & c_{11} & c_{13} & 0 & 0 & 0 \\ c_{13} & c_{13} & c_{33} & 0 & 0 & 0 \\ 0 & 0 & 0 & c_{44} & 0 & 0 \\ 0 & 0 & 0 & 0 & c_{44} & 0 \\ 0 & 0 & 0 & 0 & 0 & (c_{11}-c_{12})/2 \end{bmatrix}
\begin{Bmatrix} \varepsilon_{11} \\ \varepsilon_{22} \\ \varepsilon_{33} \\ 2\varepsilon_{23} \\ 2\varepsilon_{31} \\ 2\varepsilon_{12} \end{Bmatrix} -
\begin{bmatrix} 0 & 0 & e_{31} \\ 0 & 0 & e_{31} \\ 0 & 0 & e_{33} \\ 0 & e_{15} & 0 \\ e_{15} & 0 & 0 \\ 0 & 0 & 0 \end{bmatrix}
\begin{Bmatrix} E_1 \\ E_2 \\ E_3 \end{Bmatrix}, \text{ (S3)}
$$

$$
\begin{Bmatrix} D_1 \\ D_2 \\ D_3 \end{Bmatrix} =
\begin{bmatrix} 0 & 0 & 0 & 0 & e_{15} & 0 \\ 0 & 0 & 0 & e_{15} & 0 & 0 \\ e_{31} & e_{31} & e_{33} & 0 & 0 & 0 \end{bmatrix}
\begin{Bmatrix} \varepsilon_{11} \\ \varepsilon_{22} \\ \varepsilon_{33} \\ 2\varepsilon_{23} \\ 2\varepsilon_{31} \\ 2\varepsilon_{12} \end{Bmatrix} +
\begin{bmatrix} k_{11} & 0 & 0 \\ 0 & k_{22} & 0 \\ 0 & 0 & k_{33} \end{bmatrix}
\begin{Bmatrix} E_1 \\ E_2 \\ E_3 \end{Bmatrix}, \qquad \text{(S4)}
$$

where σ_{ij}, ε_{ij}, E_i, D_i represent the stress, strain, electrical field and electrical displacement, respectively, and c_{ij}, e_{ij}, k_{ij} are the elastic, piezoelectric and dielectric

parameters of the material. The subscript "3" denotes the polarization (vertical, Supplementary Fig. S11) direction of the PZT layer.

When subjected to the actuator voltage U_A the electric field intensity in polarization direction is $E_3 = U_A/h_{PZT}$, where h_{PZT} is the thickness of the PZT layer. For plane-strain deformation $\varepsilon_{22} = \varepsilon_{12} = \varepsilon_{23} = 0$, electric field boundary condition $E_1 = E_2 = 0$ and the approximate traction-free condition $\sigma_{33} = 0$ (by neglecting the traction from the softer substrate), equation (S3) gives

$$
\begin{cases}
\sigma_{11} = \dfrac{\left(c_{11}c_{33} - c_{13}^2\right)\varepsilon_{11} + \left(c_{13}e_{33} - c_{33}e_{31}\right)E_3}{c_{33}} \\[3mm]
\sigma_{22} = \dfrac{\left(c_{12}c_{33} - c_{13}^2\right)\varepsilon_{11} + \left(c_{13}e_{33} - c_{33}e_{31}\right)E_3}{c_{33}} \\[3mm]
\varepsilon_{33} = \dfrac{e_{33}E_3 - c_{13}\varepsilon_{11}}{c_{33}}
\end{cases}
. \tag{S5}
$$

Under bending the strain ε_{11} can be written as $\varepsilon_{11} = \kappa z + \varepsilon_{11}^0$, where the curvature κ and membrane strain ε_{11}^0 are determined by the requirement of vanishing membrane force and bending moment, i.e.,

$$
\sum_k^n F_k = \sum_k^n \int_{h_k} \overline{E}_k \varepsilon_{11} dz = 0, \quad \sum_k^n M_k = \sum_k^n \int_{h_k} \overline{E}_k \varepsilon_{11} z dz = 0. \tag{S6}
$$

The normal strain along polarization direction in the kth layer can be expressed as

$$
\varepsilon_{33} = -v_k' \varepsilon_{11}, \tag{S7}
$$

4

where $v_k' = v_k/(1-v_k)$ is the plane-strain Possion's ratio of the kth layer. The expansion of the actuator, $\Delta u = \beta_1 \cdot U_A \cdot e_{33}/c_{33}$ (equation (1) in the main text), is obtained by the integration of ε_{33}, where the dimensionless parameter β_1 depends on the material and thickness of the multilayer structure discussed above, and $\beta_1 = 1.420 \times 10^5$ for the material and dimensions in Supplementary Fig. S11.

Supplementary Note 3: Interfacial Crack and Sensor Output Voltage

As shown in Supplementary Fig. S7c, the air-gaps form at each terminal of the PZT actuator/sensor after the contact of the elastomer and prepared substrate. The actuator/sensor with two terminals can be modeled as an interfacial crack, and all the cracks are collinear. The displacement boundary conditions are given in the main text. As mentioned in the "Methods" section, the actuators and sensors consist of elastomer substrate (silicone)/bottom encapsulation (PI)/bottom electrodes/PZT/top electrodes/top encapsulation (PI) (Supplementary Fig. S34). The area of the bottom encapsulation is about 2.5 times as large as that of the top encapsulation. Therefore the effective modulus of the elastomer layer is much larger than that of the prepared substrate, and does not appear in the analysis according to interfacial fracture mechanics[2].

The collinear interfacial cracks with the boundary conditions are solved analytically by approximating the stress over each actuator/sensor by its average stress. This gives the average stress on the ith sensor, $p_{S,i} = \eta_i \cdot \Delta u \cdot E_{P.S.}/2a$ (equation (2) in the main text), where the parameter η_i is dimensionless, and $\eta_1 = 1.072 \times 10^{-2}$,

$\eta_2 = 3.098 \times 10^{-3}$, $\eta_3 = 1.114 \times 10^{-3}$, $\eta_4 = 5.683 \times 10^{-4}$, $\eta_5 = 3.437 \times 10^{-4}$ and

$\eta_6 = 2.300 \times 10^{-4}$ for the positions in Fig. 1f. For the pressure $p_{S,i}$ on the ith sensor and

the stress and electric displacement fields $\sigma_{33}^i = p_{S,i}$ and $D_3^i = 0$ (where the superscript

"i" denotes the ith sensor) , equations (S3) and (S4) give

$$\begin{cases} \sigma_{11}^i = c_{11}\varepsilon_{11}^i + c_{13}\varepsilon_{33}^i - e_{31}E_3^i \\ p_{S,i} = c_{13}\varepsilon_{11}^i + c_{33}\varepsilon_{33}^i - e_{33}E_3^i, \\ 0 = e_{31}\varepsilon_{11}^i + e_{33}\varepsilon_{33}^i + k_{33}E_3^i \end{cases} \tag{S8}$$

Similar to Supplementary Note 2, the strain ε_{11}^i can be written as $\varepsilon_{11}^i = \kappa_i z + \left(\varepsilon_{11}^0\right)_i$, where

the curvature κ_i and membrane strain $\left(\varepsilon_{11}^0\right)_i$ are determined by the requirement of

vanishing membrane force and bending moment in equation (S6). Equation (S8) then

give the strains (ε_{11}^i and ε_{33}^i) and the electric field intensity (E_3^i). The output voltage of

the ith sensor is obtained in the main text as $U_{S,i} = \beta_2 \cdot p_{S,i} \cdot h_{PZT}/e_{33}$ (equation (3)), where

the dimensionless parameter β_2 depends on the material and geometry of the multilayer

structure, and $\beta_2 = 3.467 \times 10^{-3}$ for the material and dimensions in Supplementary Fig.

S11. For plane-strain deformation $\varepsilon_{22} = \varepsilon_{12} = \varepsilon_{23} = 0$ and $\sigma_{33}^i = p_{S,i}$ (in the kth layer), the

normal strain along polarization direction in the kth layer can be expressed as

$\left(\varepsilon_{33}^i\right)_k = \left[1 - \left(v_k'\right)^2\right] p_{S,i}/\overline{E}_k - v_k'\varepsilon_{11}^i$, where $\overline{E}_k$ and v_k' are plane-strain modulus and

Possion's ratio, respectively (see Supplementary Note 2 and 3). The expansion $\Delta u_{s,i}$ of

the ith sensor is obtained by integrating of $\left(\varepsilon_{33}^i\right)_k$ as

$$\Delta u_{S,i} = \zeta_i \frac{e_{33}}{c_{33}} U_A,$$ (S9)

where the parameter ζ_i is dimensionless, and $\zeta_1 = -2.135 \times 10^{-2}$, $\zeta_2 = -6.172 \times 10^{-3}$, $\zeta_3 = -2.220 \times 10^{-3}$, $\zeta_4 = -1.132 \times 10^{-3}$, $\zeta_5 = -6.849 \times 10^{-4}$ and $\zeta_6 = -4.583 \times 10^{-4}$ for the positions in Fig. 1f. From equation (1) (in the main text) and equation (S9), the ratio of expansion of the active actuator to that of any other sensors is in the range

$$\left| \Delta u / \Delta u_{S,i} \right| = \left| \beta_1 / \zeta_i \right| = 6.651 \times 10^6 : 3.098 \times 10^8.$$

For a substrate with the Young's modulus determined by DMA, the output voltage of the most left sensor, obtained from equation (4) in the main text, agrees well with the measured values from experiments (Fig. 2a) for the actuator voltage ranging from 2 V to 5 V with an increment of 1 V.

The effect of shear stress at the device/prepared substrate interface is studied by comparing the experiment for the bare device (without the PDMS sample) to that for the substrate and PDMS sample having the same moduli. For the former (no PDMS sample) there is no crack opening such that any measured sensor voltage would result from the interfacial shear. For the latter, the effect of interfacial shear is the same as that for the former (because the PDMS sample has the same moduli as the substrate), but the crack opening due to expansion of actuator/sensor comes into play. In fact, its sensor voltage in experiments is much larger (by orders of magnitude) than that from the bare device (without PDMS sample) case. This clearly shows that the effect of interfacial shear is indeed negligible as compared to that for crack to opening (unless there is only bare

device). This is consistent with the prior analyses of stiff devices on compliant substrates[3-6].

Supplementary Note 4: Viscoelastic Analysis

The relaxation modulus of PDMS can be expressed via Prony series in time domain[7,8]

$$E(t) = E_0 \left[1 - \sum_{i=1}^{N} g_i \left(1 - e^{-t/\tau_i} \right) \right],$$ (S10)

where E_0 represents the initial modulus, g_i, τ_i and N are the parameters and number of terms in the Prony series. The limit of $E(t \to \infty)$ gives the fully relaxed modulus

$E_\infty = E_0 \left(1 - \sum_{i=1}^{N} g_i \right)$. The Laplace transform gives the frequency-dependent relaxation modulus,

$$E(\omega) = E_\infty \frac{1 - \sum_{i=1}^{N} \frac{g_i}{1 + \tau_i^2 \omega^2} + j \sum_{i=1}^{N} \frac{g_i \tau_i \omega}{1 + \tau_i^2 \omega^2}}{1 - \sum_{i=1}^{N} g_i},$$ (S11)

where, $j = \sqrt{-1}$, and $\omega = 2\pi f$ is the angular frequency. The real and imaginary parts of the above equation represent the storage and loss moduli, respectively. The phase shift is defined by $\tan \delta = E_{loss}/E_{storage}$. The relaxation ratio ($g_i$) has been reported in the literature[9,10], g_1=0.137, g_2=0.0921, and g_3=0.315. The relaxation time (τ_i) is determined in the main text, which gives τ_1=0.0235s, τ_2=0.00165s, and τ_3=0.000281s. As shown in

8

Supplementary Fig. S34, the PI layer for the bottom encapsulation (between the elastomer substrate (silicone) and the PZT actuators/sensors) is much larger than that for the top encapsulation. The elastic modulus of PI is 5 orders of magnitude larger than that of the elastomer layer. Therefore, the bottom encapsulation may shield the viscoelastic effect of the device substrate on the output of the device.

Supplementary Note 5: Conformal Contact

The surface profile of the skin can be generally represented by[1]

$$w(x) = \frac{h_{skin}}{2}\left[1 + \cos\left(\frac{2\pi x}{\lambda_{skin}}\right)\right],$$ (S12)

where h_{skin} and λ_{skin} represent the roughness and wavelength of the skin, respectively. Since the skin is much more compliant than the device, it conforms to the device, which leads to the normal traction on the skin surface[11]

$$T(x) = \frac{\pi \bar{E}_{skin} h_{skin}}{2\lambda_{skin}} \cos\left(\frac{2\pi x}{\lambda_{skin}}\right),$$ (S13)

where $\bar{E}_{skin}$ represents the plane-strain modulus of the skin. The deformation energy (per unit length) of the skin is

$$\bar{U}_{skin} = \frac{1}{\lambda_{skin}} \int_0^{\lambda_{skin}} T(x) w(x) dx = \frac{\pi \bar{E}_{skin} h_{skin}^2}{8\lambda_{skin}}.$$ (S14)

The adhesion energy (per unit length) is[1]

$$\bar{U}_{adhesion} = -\frac{\gamma}{\lambda_{skin}} \int_0^{\lambda_{skin}} \sqrt{1+(w')^2}\,dx \approx -\gamma\left(1+\frac{\pi^2 h_{skin}^2}{4\lambda_{skin}^2}\right), \tag{S15}$$

where γ is the work of adhesion between the skin and the device. The total energy is obtained from equations (S14) and (S15) as

$$\bar{U}_{total} = \frac{\pi \bar{E}_{skin} h_{skin}^2}{8\lambda_{skin}} - \gamma\left(1+\frac{\pi^2 h_{skin}^2}{4\lambda_{skin}^2}\right). \tag{S16}$$

Conformal contact of the device and skin requires the total energy less than zero, its value for unadhered state, i.e., $\bar{U}_{total} < 0$, which gives the maximum roughness for conformal contact

$$\left(\frac{1}{8}-\frac{\pi\gamma}{4\lambda_{skin}\bar{E}_{skin}}\right)h_{skin}^2 \leq \frac{\gamma\cdot\lambda_{skin}}{\pi\bar{E}_{skin}}. \tag{S17}$$

For the skin roughness[12] $h_{skin}=5\sim10\mu m$, $\lambda_{skin}\approx7h_{skin}$, $\bar{E}_{skin}\approx130KPa$ and equation (S17) clearly holds such that the device and skin have intimate contact, and the device remains essentially flat. Therefore, the sensor's output voltage is independent of the roughness of the skin.

References

1. Wang, S. *et al.* Mechanics of Epidermal Electronics. *J. Appl. Mech.* **79,** 031022–031022 (2012).

2. Suo, Z. Singularities interacting with interfaces and cracks. Int. J. Solids Struct. **25**(10), 1133–1142 (1989).

3. Khang, D.Y., Jiang, H.Q., Huang, Y., Rogers, J.A. A stretchable form of single-crystal silicon for high-performance electronics on rubber substrates. *Science*. **311**(5758), 208-212 (2006).

4. Jiang, H.Q., Khang, D.Y., Song, J.Z., Sun, Y.G., Huang, Y.G., Rogers, J.A. Finite deformation mechanics in buckled thin films on compliant supports. *P. Natl. Acad. Sci. USA*. **104**(40), 15607-15612 (2007).

5. Song, J.Z., Jiang, H.Q., Liu, Z.J., Khang, D.Y. Huang, Y., Rogers, J.A., Lu, C., Koh, C.G. Buckling of a stiff thin film on a compliant substrate in large deformation. *Int. J. Solids Struct*. **45**(10) 3107-3121 (2008).

6. Huang, Z.Y., Hong, W., Suo, Z. Nonlinear analyses of wrinkles in a film bonded to a compliant substrate. *J. Mech. Phys. Solids*. **53**(9), 2101-2118 (2005).

7. Christensen, R.M., Theory of Viscoelasticity. *Acad. Press N. Y.* (1982).

8. Lakes, R.S., Viscoelastic Solids. *CRC Press Fla.* (1998).

9. Cheng, H., Li, M., Wu, J. *et al.* A Viscoelastic Model for the Rate Effect in Transfer Printing. *J. Appl. Mech-T ASME.* 80(4), 041019 (2013).

10. Lin, I.K., Liao, Y.M., Liu, Y. *et al*. Viscoelastic mechanical behavior of soft microcantilever-based force sensors. *Appl. Phys. Lett.* **93**(25) 251907 (2008).

11. Jiang, H., Sun, Y., Rogers, J. A. & Huang, Y. Post-buckling analysis for the precisely controlled buckling of thin film encapsulated by elastomeric substrates. *Int. J. Solids Struct.* **45,** 3858–3867 (2008).

12. Kim, D.-H. *et al.* Epidermal Electronics. *Science* **333,** 838–843 (2011).
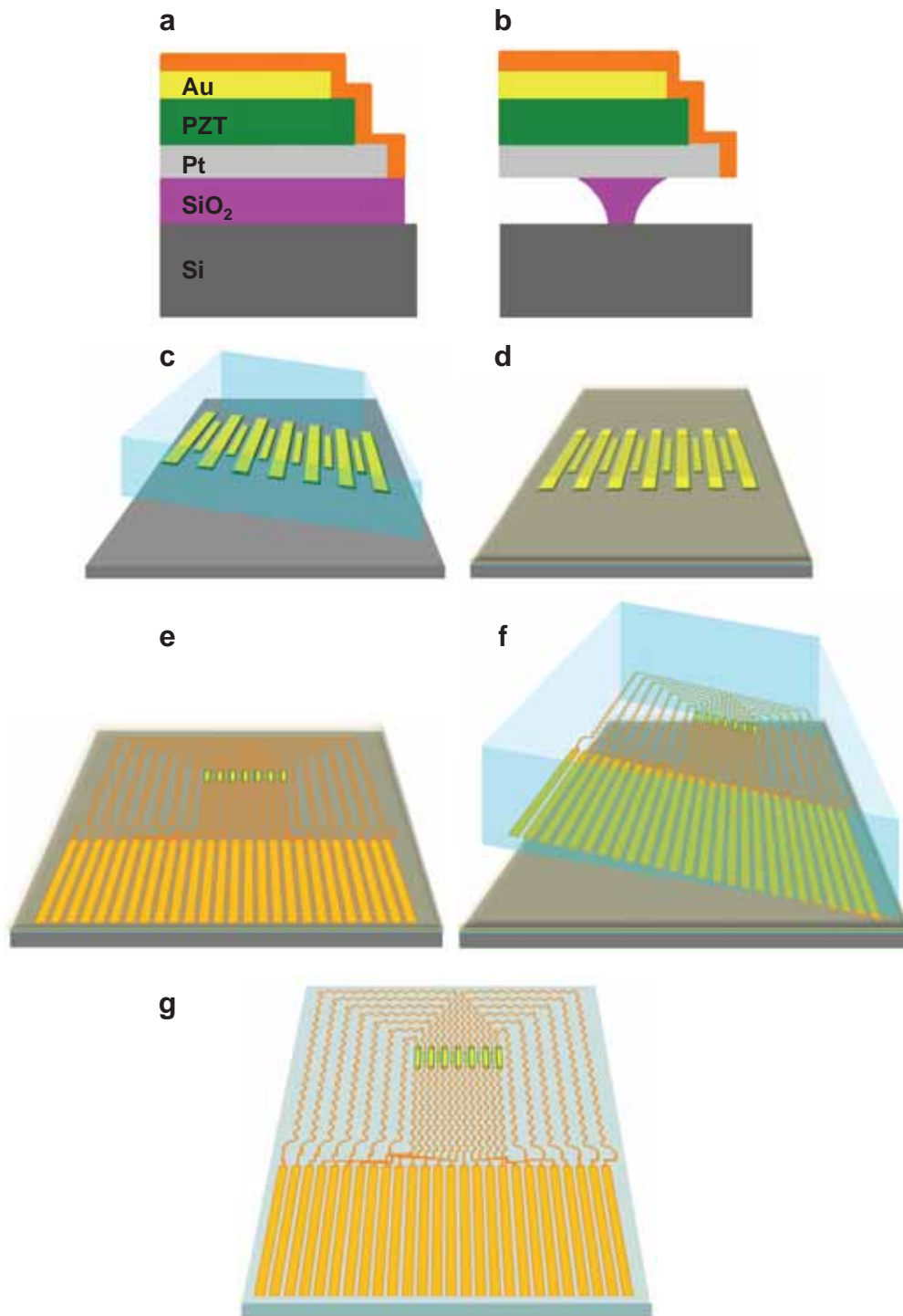
Supplementary Figure S1. Schematic illustration of procedures for fabricating a PZT CMS on a silicone substrate. (a) Cross sectional illustration of the edge of a single PZT nanoribbon in a capacitor structure on an SiO_2/Si wafer. **(b)** Cross sectional illustration of the same region an intermediate state of undercut etching with dilute HF solution. **(c)** Process of retrieving the PZT sensor and actuator arrays with a PDMS stamp, leaving them adhered to the surface of the stamp. **(d)** Result after transfer printing onto a temporary substrate. **(e)** Completed CMS system on temporary substrate, at a reduced magnifiation view. **(f)** Process of retrieving the system with a PDMS stamp. **(g)** Result after transfer printing onto a thin silicone substrate.
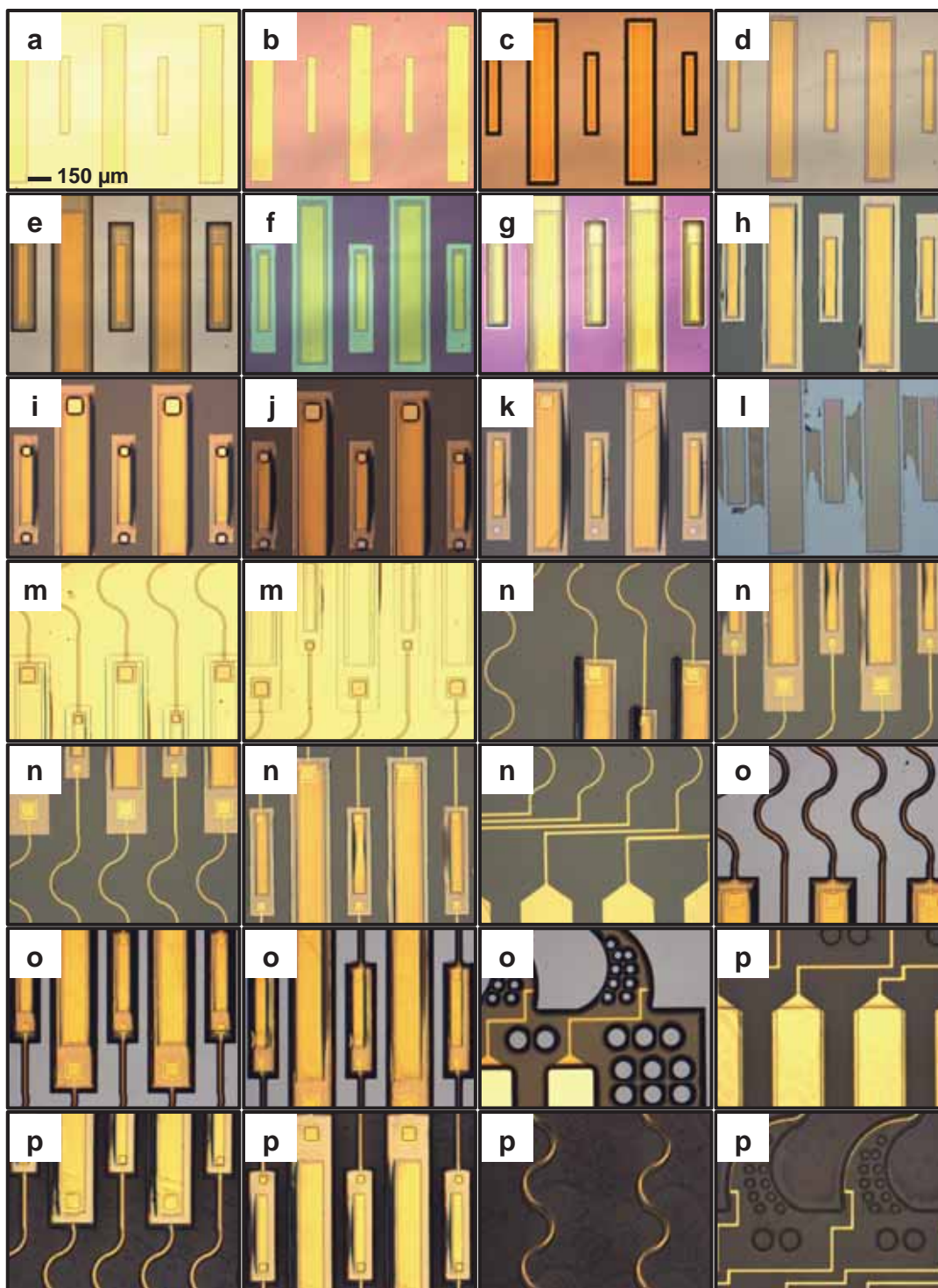
Supplementary Figure S2. Optical micrographs of key structures at various stages of fabricating the CMS systems. Optical microscope image of **(a)** photoresist patterned on gold (Au) to define electrodes for capacitor structures, **(b)** pattern of Au formed by etching, **(c)** photoresist patterned for etching the underlying layer of PZT, **(d)** PZT layer after selective etching, **(e)** photoresist patterned for etching the underlying layer of Pt, **(f)** Pt layer after selective etching, **(g)** photoresist patterned for undercuttting the SiO_2 layer with diluted HF, **(h)** structure after etching with HF, **(i)** photoresist patterned for defining contact holes through the polyimide (PI), **(j)** pattern after etching the PI, **(k)** PZT sensor and actuator arrays on a temporary substrate, **(l)** remaining materials on the temporary substrate after retrieving the arrays with a PDMS stamp, **(m)** photoresist patterned on Au to define serpentine interconnections to the arrays, **(n)** serpentine interconnections formed by etching the Au, **(o)** photoresist patterned mask for defining the PI encapsulation, **(p)** pattern of the arrays with serpentine interconnections after etching PI.
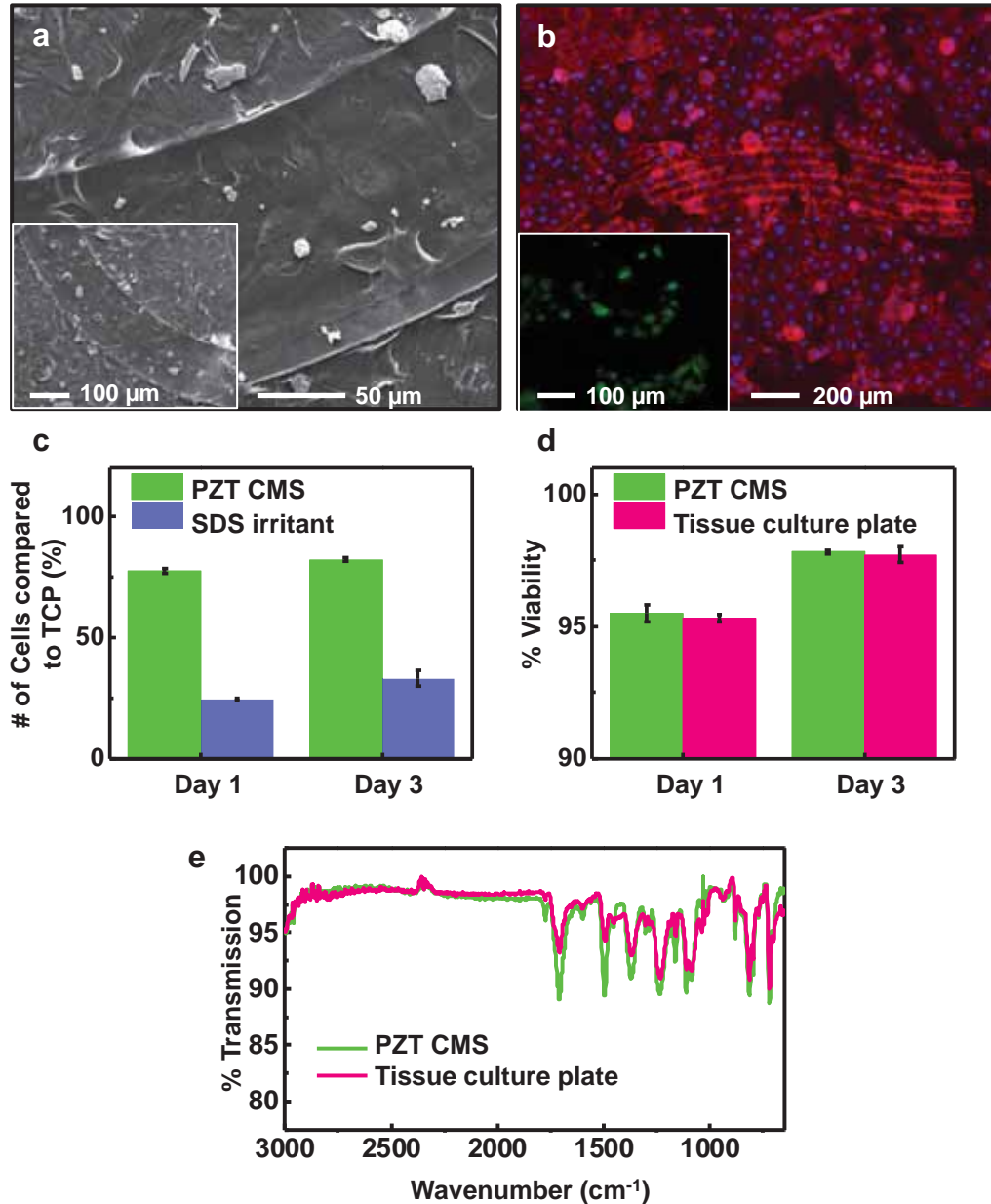
Supplementary Figure S3. Human epithelial keratinocyte (HEK) biocompatibility tests for PZT CMS.
(a) SEM images of HEK on a device after 24 hours of culture. **(b)** Optical micrographs showing Actin (red) and DAPI (blue) staining of HEK on a device following 24 hours of culture and Live (green)/Dead (red) staining (inset). **(c)** MTT assay of HEK on a device after 1 and 3 days of culture as a percentage of cells grown on tissue culture plate. Cells incubated with 5% SDS served as a positive control. **(d)** Cell viability on a device and on a tissue culture plate after 1 and 3 days of culture. **(e)** ATR-FTIR collected on a device before and after 7 days incubation with cells. The spectra exhibit no significant change.
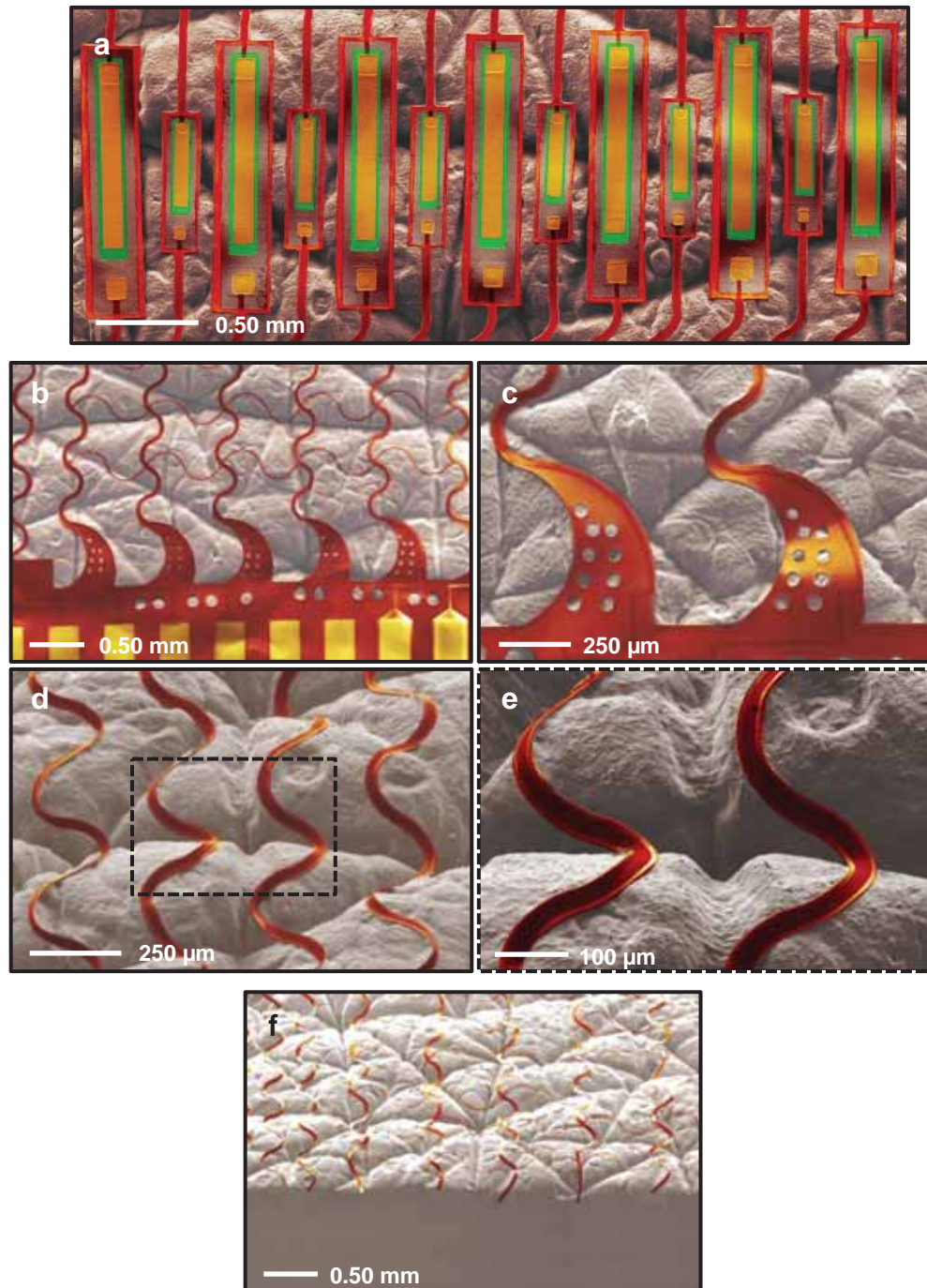
Supplementary Figure S4. Colorized SEM images of a representative PZT CMS device on an artificial skin surface. (a) PZT sensors and actuators, where the RGB values for the various layers are as follows: Gold (218, 165, 32), PZT (57, 206, 72), PI (243. 111. 39), Skin (190, 142, 122). **(b,c)** Pads for connection to anisotropic conductive films. **(d)** Serpentine interconnections. **(e)** Magnified view of the region identified by the black dashed box in **d**. **(f)** Low magnification image serpentine interconnections, collected with a tilt angle of 45^0.
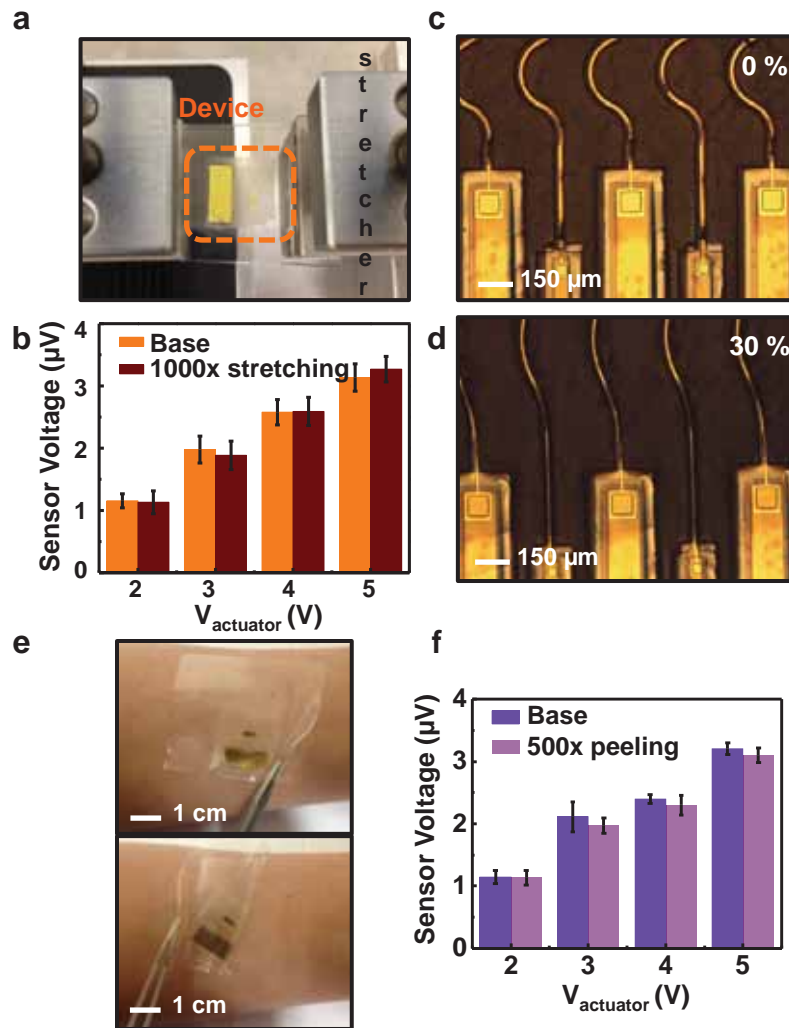
Supplementary Figure S5. Characteristics of a PZT CMS under cyclical application of tensile strain.
(a) Photograph of a PZT CMS clamped on a stretching stage. **(b)** Sensor voltage as a function of actuator voltage before (base) and after 1000 cycles of stretching to 30% tensile strain. Optical image of the sensor and actuator arrays under **(c)** 0% and **(d)** 30% stretching. **(e)** Picture of PZT CMS application on skin. **(f)** Sensor voltage as a function of actuator voltage before application onto the skin (base) and after 500 cycles of application and removal.
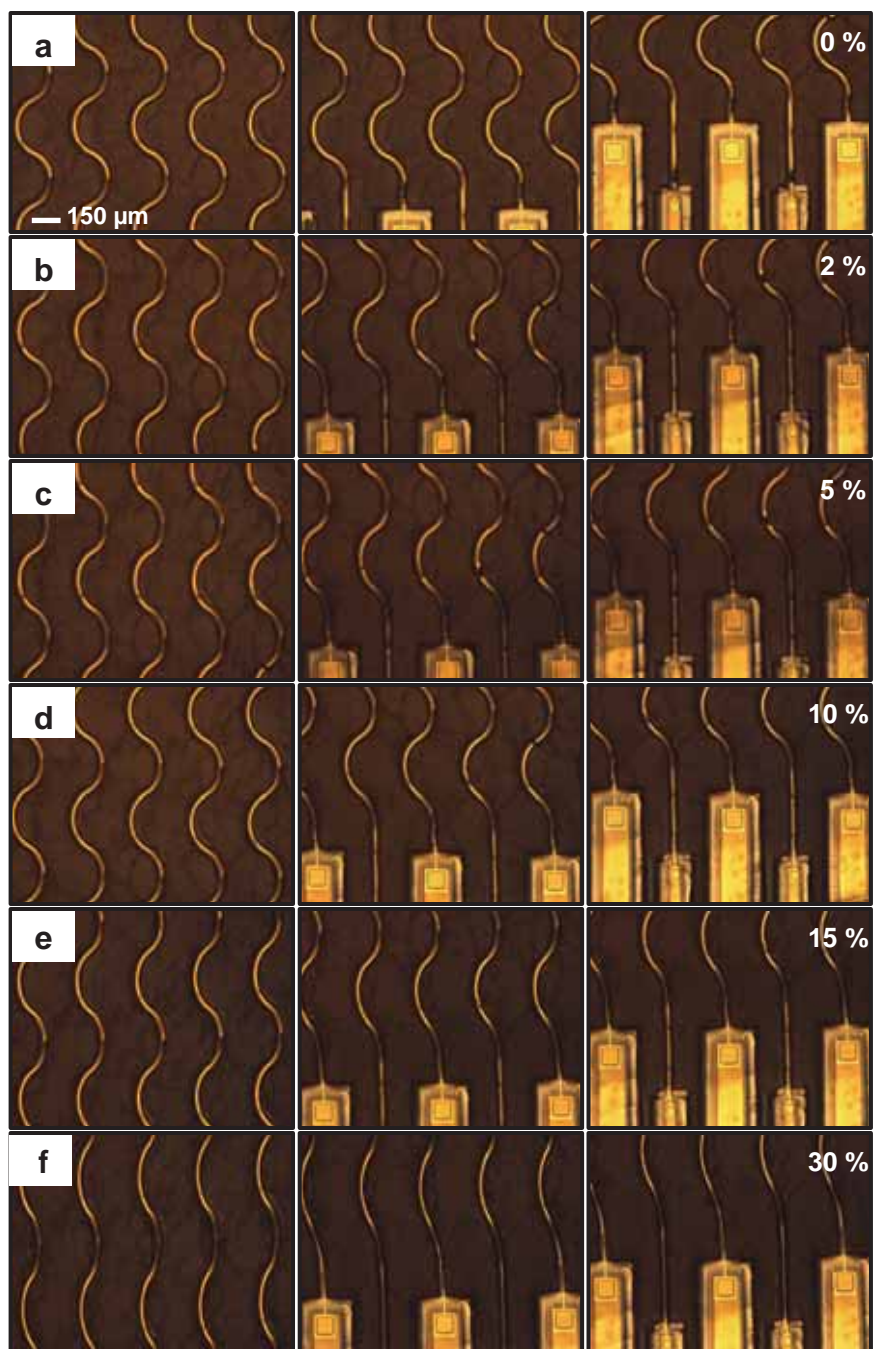
Supplementary Figure S6. Optical micrographs of serpentine interconnections and arrays of sensors and actuators at various levels of tensile strain. (a) 0%, **(b)** 2%, **(c)** 5%, **(d)** 10%, **(e)**15%, **(f)** 30%.

a

No actuating voltage   No pressure at sensors

actuator   sensor   actuator   sensor   actuator   sensor

PDMS

(Not to Scale)

b

After actuating voltage   Pressure induced by expansion $U_{sensor}\,(\text{sensor voltage}) \propto p_{sensor}\,(\text{pressure at sensor})$

PDMS

(Not to Scale)

c

Expansion of the actuator after actuating voltage

Air-gaps
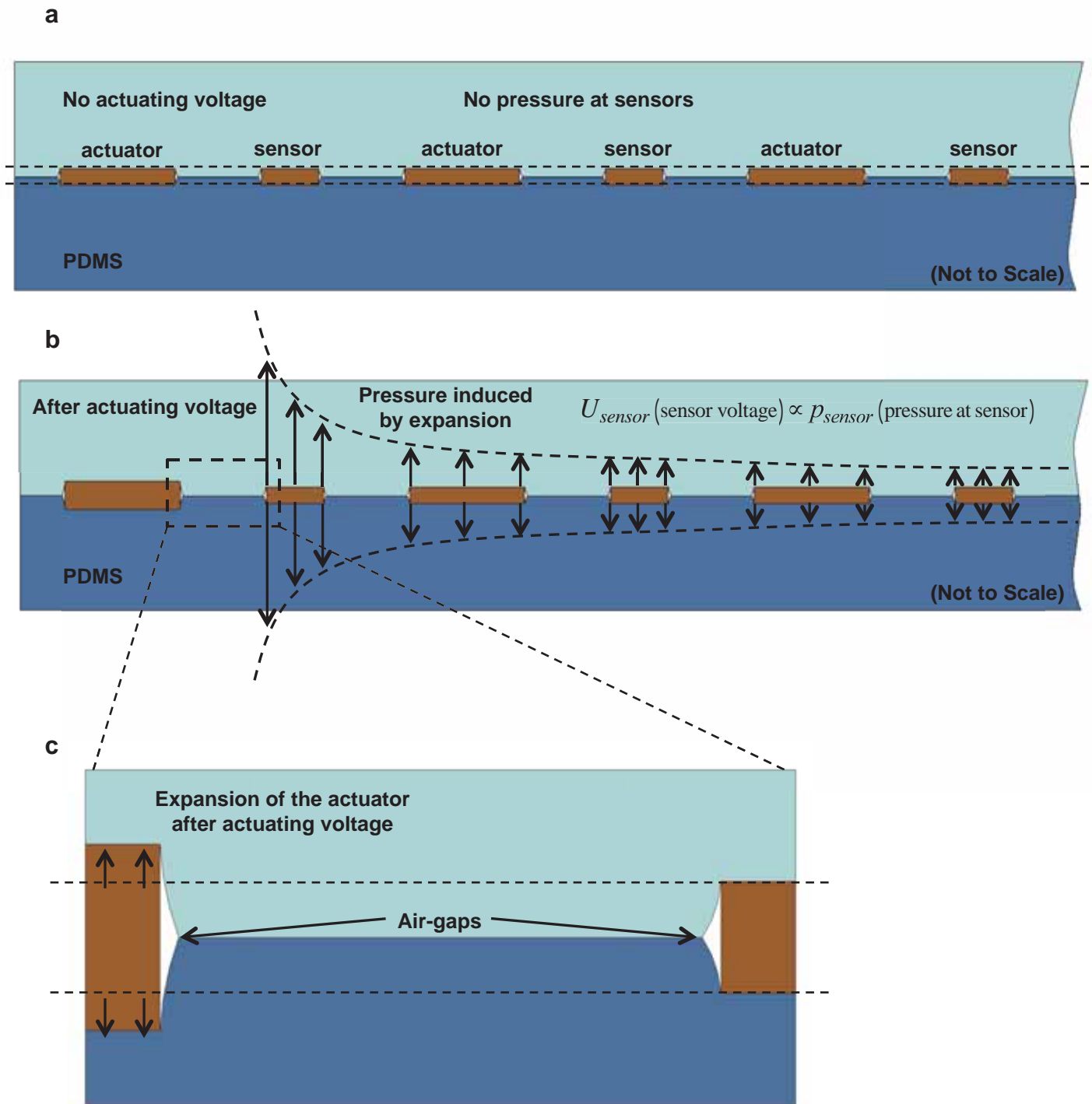
Supplementary Figure S7. Schematic cross sectional illustration of the mechanics principles associated with theoretical modeling of the device physics. (a) Initial state of the sensors and actuators at the interface between the supporting substrate (top) and the sample under test (bottom; PDMS) **(b)** Schematic distribution of pressure induced by expansion of the leftmost actuator element. **(c)** Expansion of the actuator after applying a voltage. Figures are not to scale.
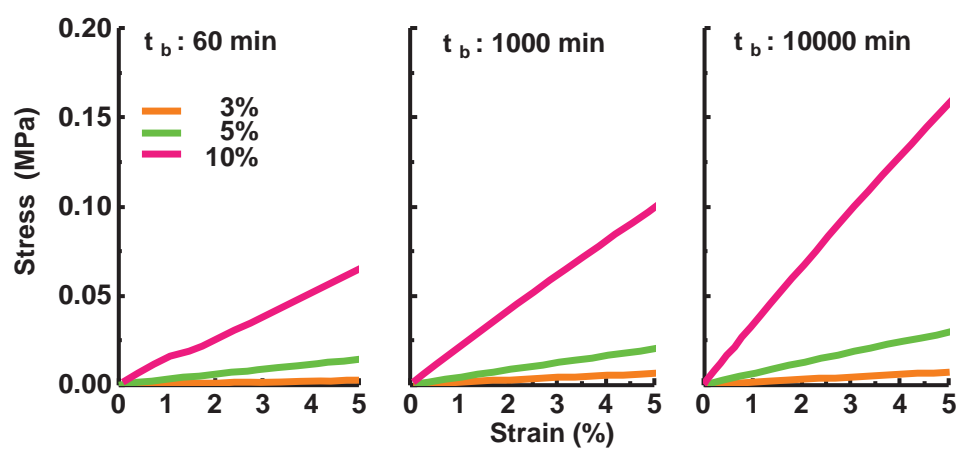
Supplementary Figure S8. Stress-strain responses measured by quasi-static dynamic mechanical analysis of various formulations of PDMS. Measurement results for different amounts of crosslinker, by weight (pink: 3%, green: 5%, blue: 10%) cured at 70 ºC for 60, 1000, and 10,000 minutes.
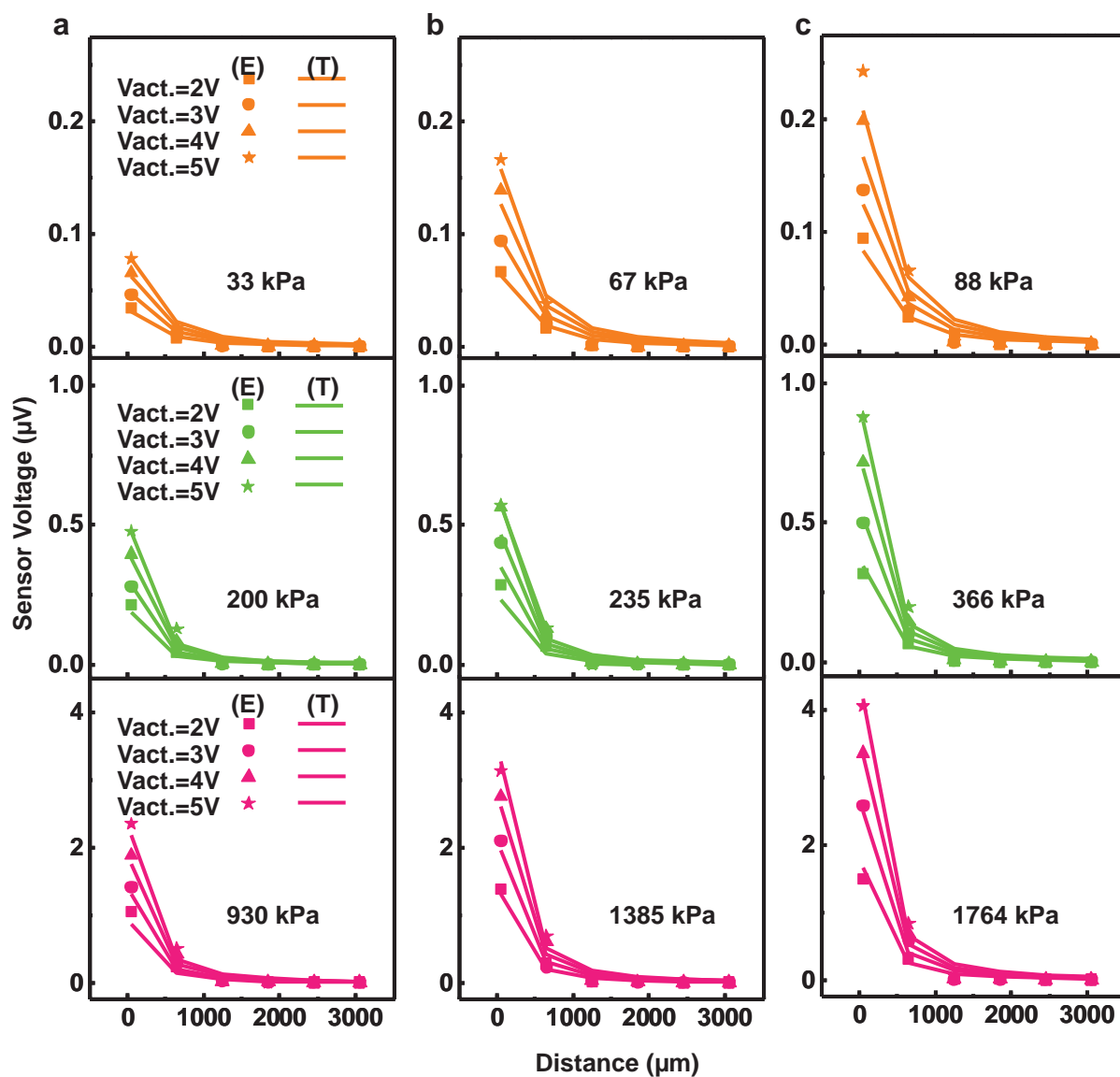
Supplementary Figure S9. Data from a PZT CMS device used for *in vitro* characterization of PDMS test samples with various modulus values. Sensor voltage as a function of distance to the actuator for samples with moduli of **(a)** 33 kPa, 200 kPa, 930 kPa, respectively, **(b)** 67 kPa, 235 kPa, 1385 kPa, respectively, **(c)** 88 kPa, 366 kPa, 1764 kPa, respectively. The experimental and theoretical results are shown as symbols and lines, respectitvely.
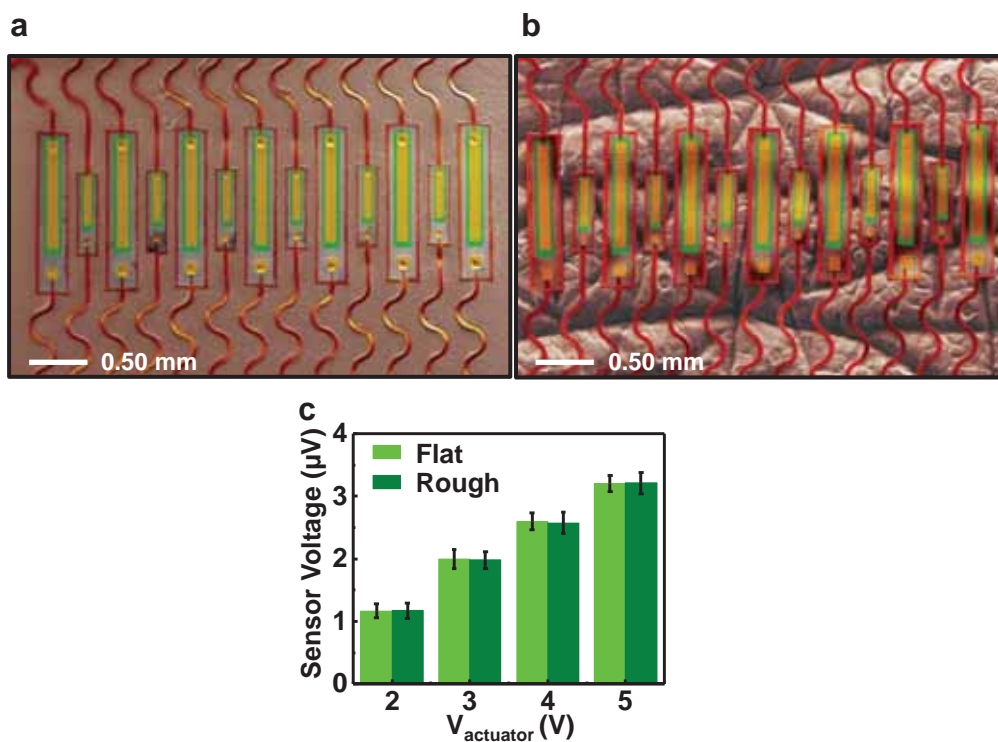
Supplementary Figure S10. SEM images of a PZT CMS on flat and rough substrates with comparisons of measurement results. (a,b) PZT CMS on flat and rough substrate, respectively. **(c)** Sensor voltage as a function of actuator voltage for the cases of flat and rough substrates. The error bars represent the standard errors.
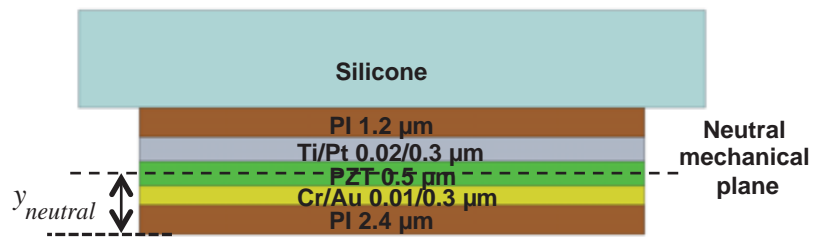
Supplementary Figure S11. Schematic cross sectional illustration of the layout of the sensors/ actuators, with the location of the neutral mechanical plane highlighted.
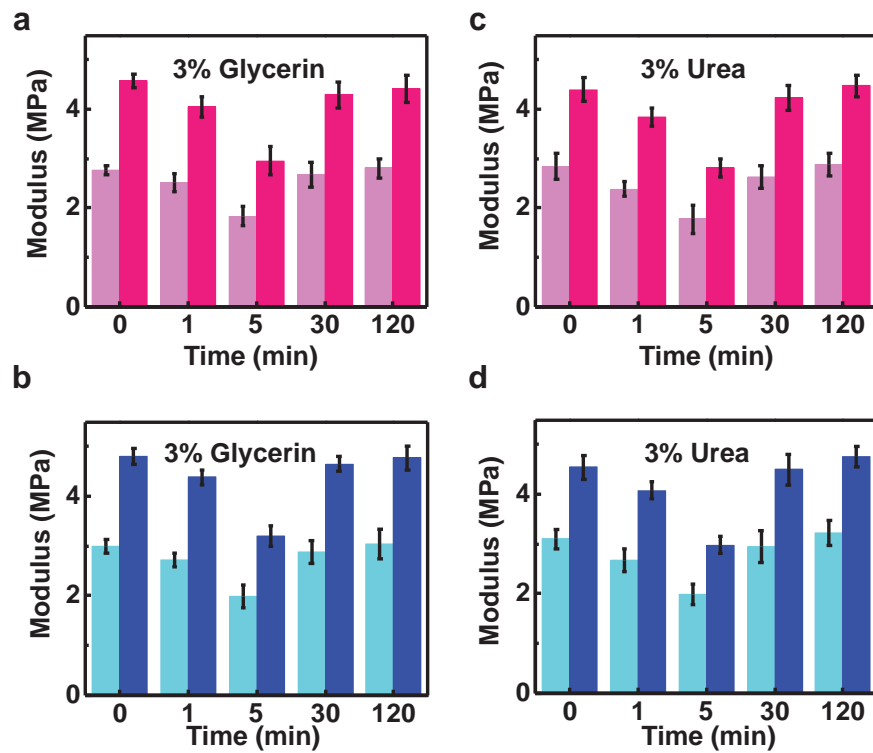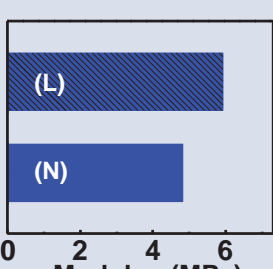
Supplementary Figure S12. *Ex vivo* evaluation of the modulus values of female and male abdominal skin before and at various time points after the application of 3% Glycerin and 3% Urea solution. Modulus values for young and old **(a)** female and **(b)** male skin, before (0 min) and at various times after application of 3% glycerin solution. Modulus values for yound and old **(c)** female and **(d)** male skin, before (0 min) and at various times after application of 3% urea solution.
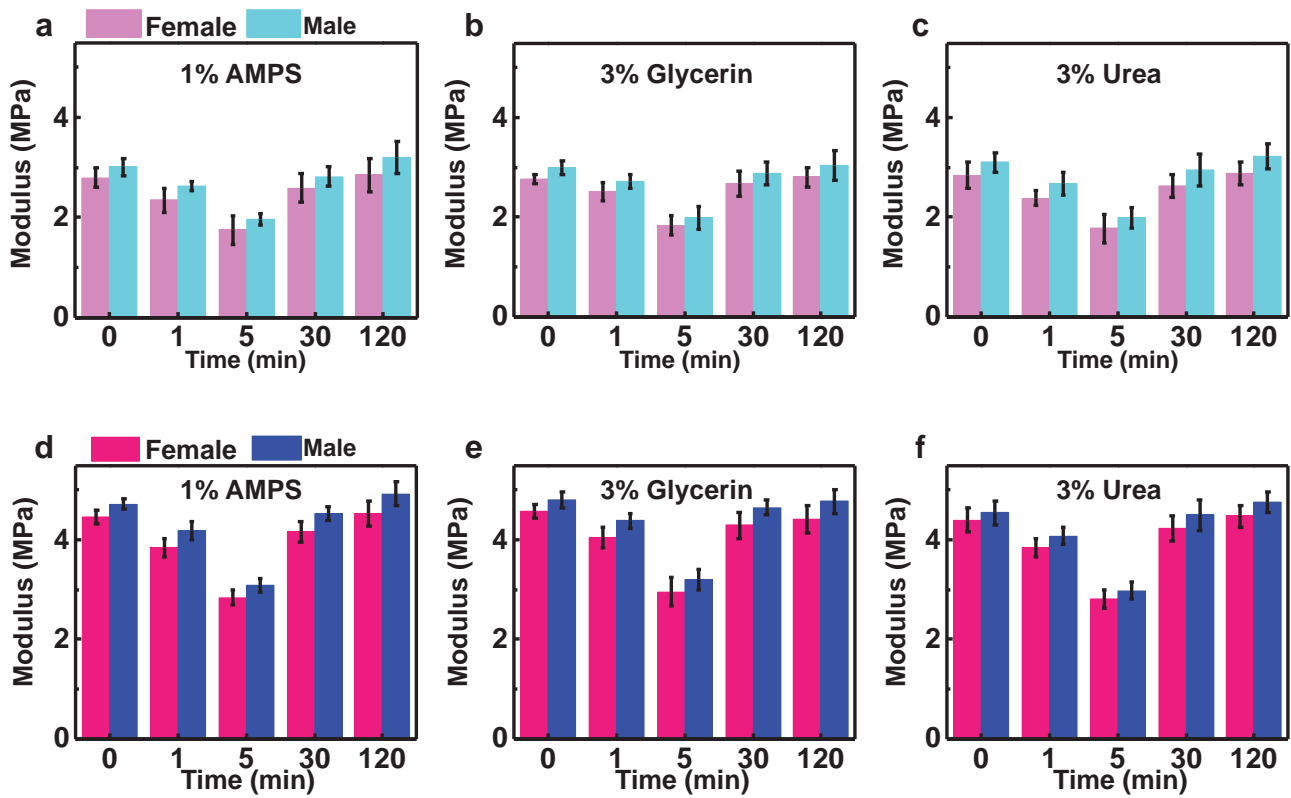
Supplementary Figure S13. *Ex vivo* evaluation of the modulus values of female and male abdominal skin before and at various time points after the application of 1% AMPS, 3% Glycerin and 3% Urea solution. Modulus values for young female and male skin before (0 min) and at various times after application of **(a)** 1% AMPS, **(b)** 3% glycerin and **(c)** 3% urea solutions. Modulus values for old female and male skin before (0 min) and at various times after application of **(d)** 1% AMPS, **(e)** 3% glycerin and **(f)** 3% urea solutions.
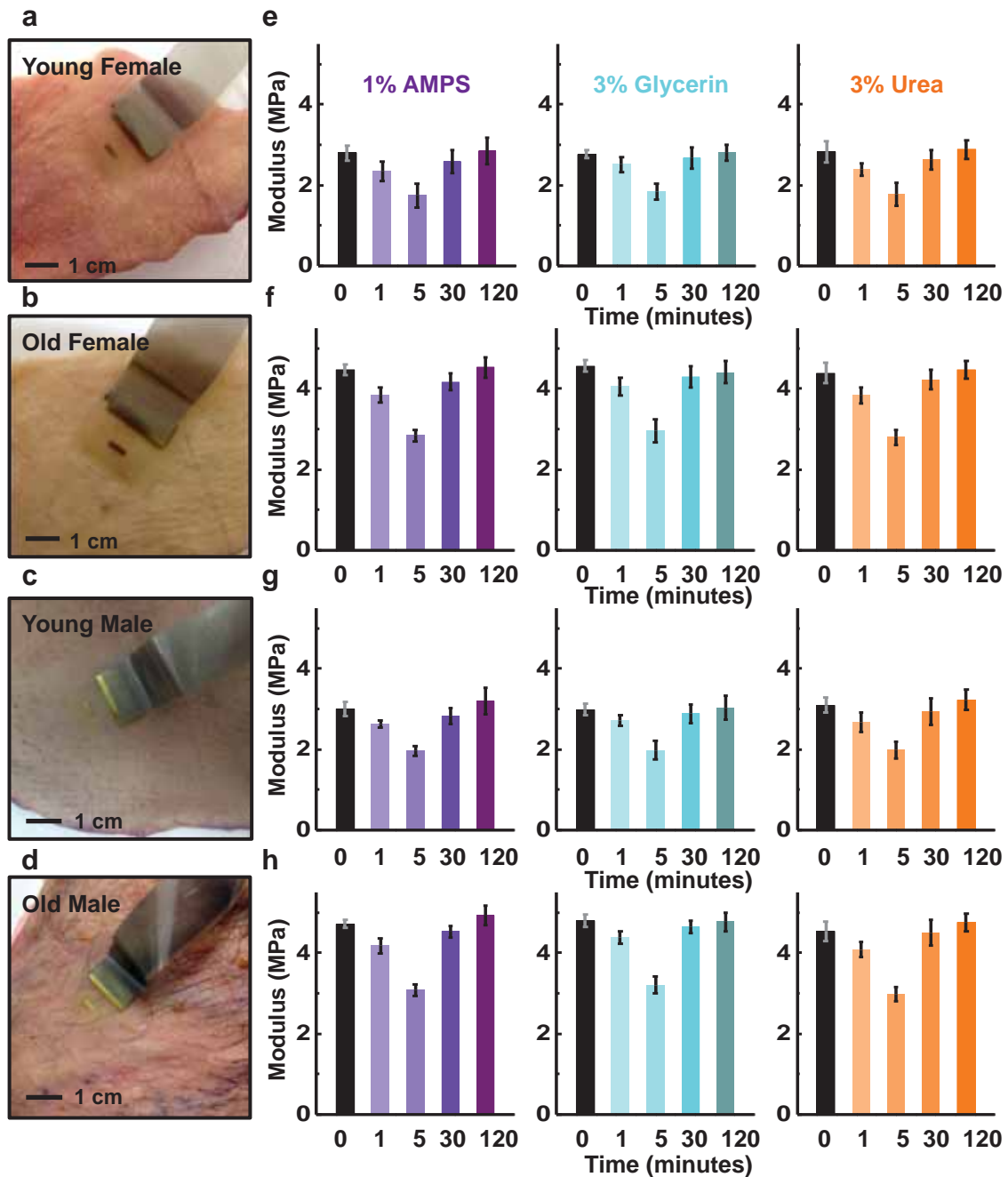
Supplementary Figure S14. *Ex vivo* **evaluation of the modulus values of female and male abdominal skin before and at various time points after the application of 1% AMPS, 3% Glycerin and 3% Urea solution.** Photograph of a device on skin from a **(a)** young female, **(b)** old female, **(c)** young male and **(d)** old male. **(e-h)** Modulus values before (0 min) and at various time after application of 1% AMPS (purple), 3% glycerin (blue) and 3% urea (orange) solutions onto the corresponding skin samples shown in **(a-d)**, respectively.
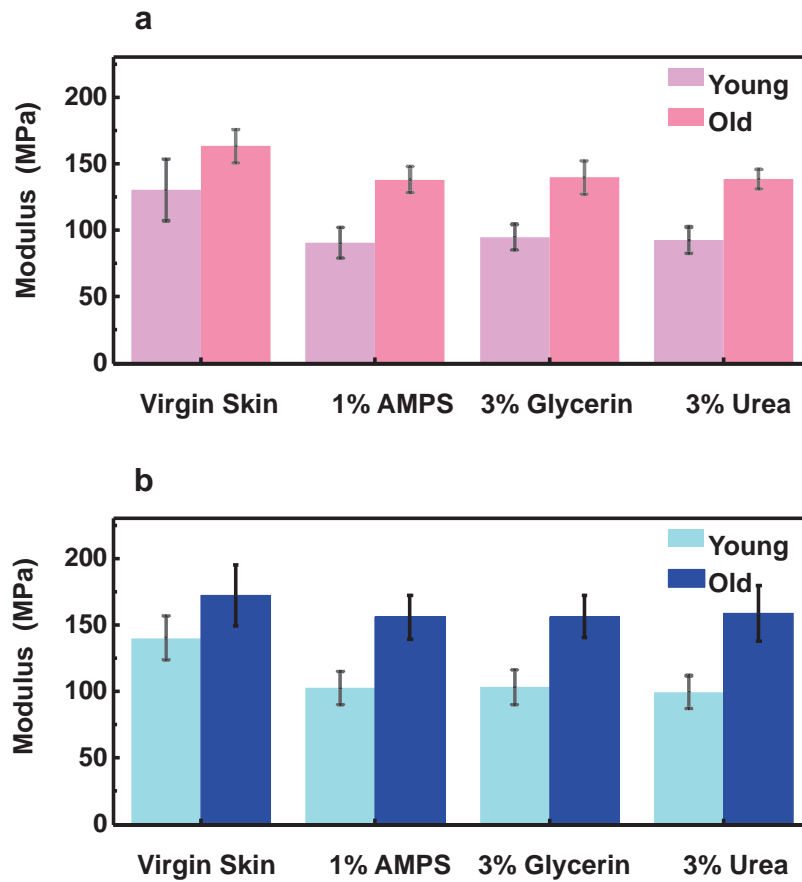
Supplementary Figure S15. Nanoindentation measurements on *ex vivo* skins. The data illustrate the effects of application of 1% AMPS, 3% Glycerin and 3% Urea solutions on the modulus of young and old **(a)** female and **(b)** male abdominal skin.
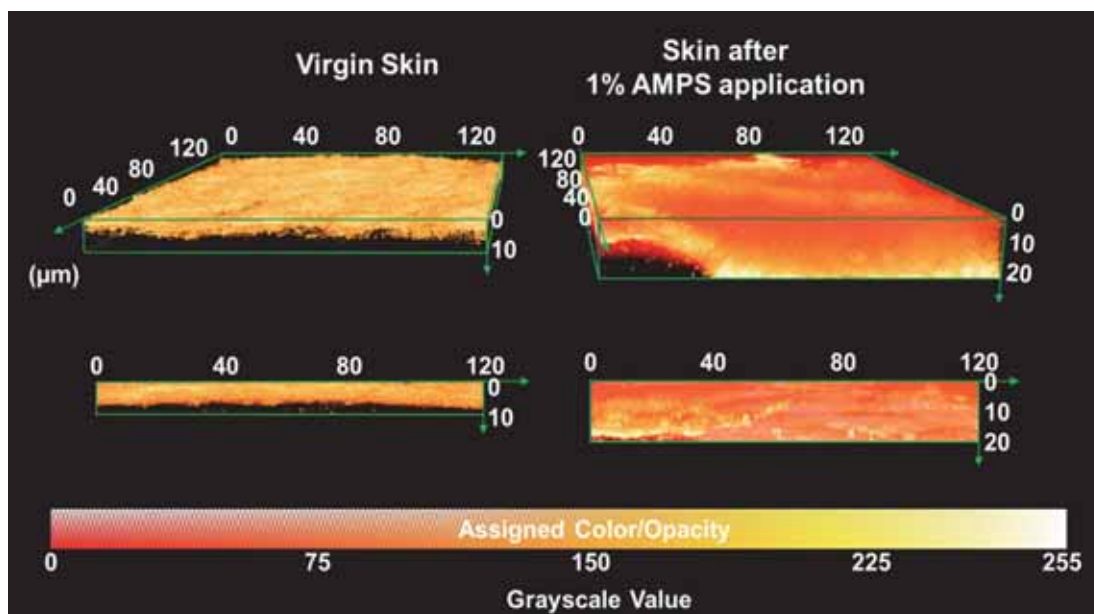
Supplementary Figure S16. Visible laser confocal microscope 3D images of *ex vivo* old female abdominal skin following the application of 1% AMPS (right images) and associated virgin skin (left images). Angled and cross-sectional views appear above and below, respectively.
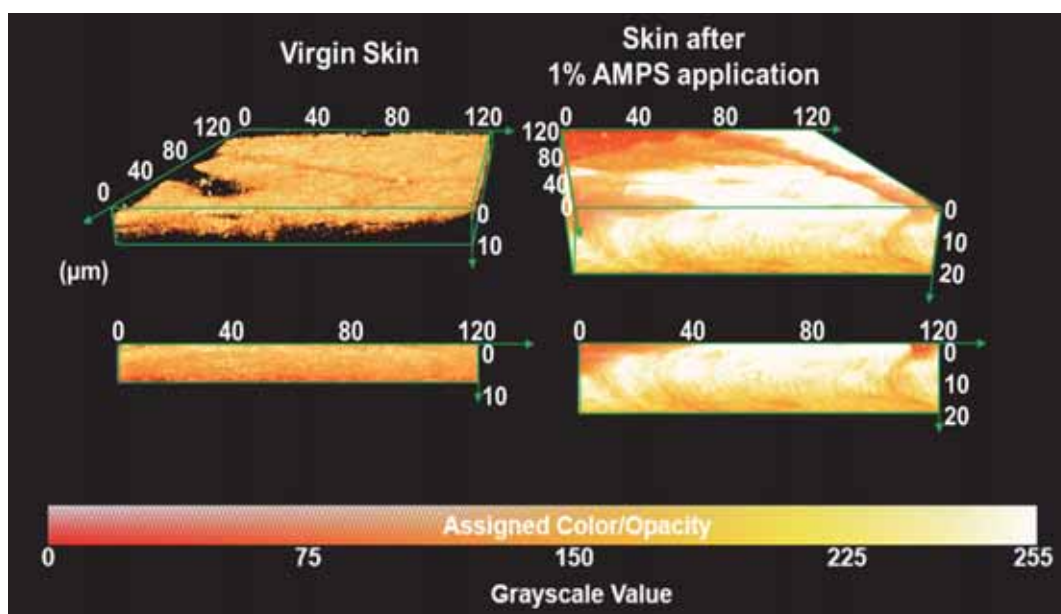
Supplementary Figure S17. Visible laser confocal microscope 3D images of *ex vivo* young male abdominal skin following the application of 1% AMPS (right images) and associated virgin skin (left images). Angled and cross-sectional views appear above and below, respectively.
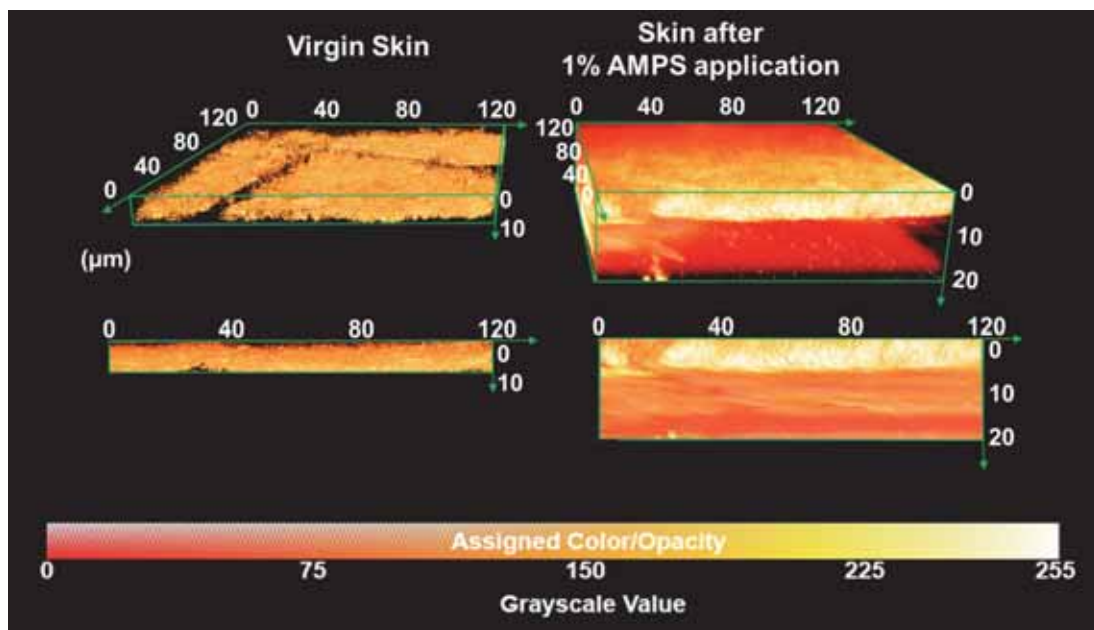
Supplementary Figure S18. Visible laser confocal microscope 3D images of *ex vivo* old male abdominal skin following the application of 1% AMPS (right images) and associated virgin skin (left images). Cross-sectional views of respective skin are presented at the bottom with associated histograms. Angled and cross-sectional views appear above and below, respectively.
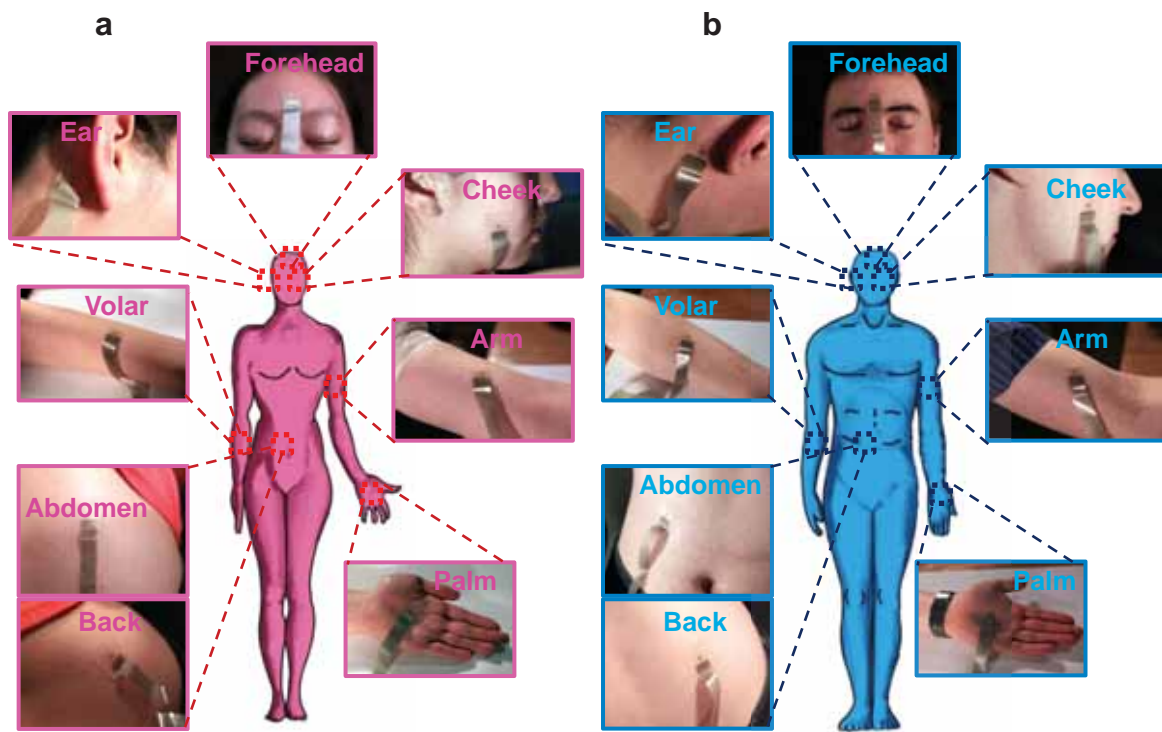
Supplementary Figure S19. Cartoon illustration of the location of *in vivo* PZT CMS measurements and associated pictures of devices on forehead, ear, forearm (volar surface), abdomen, back, palm, arm, and cheek of **(a)** female and **(b)** male body.
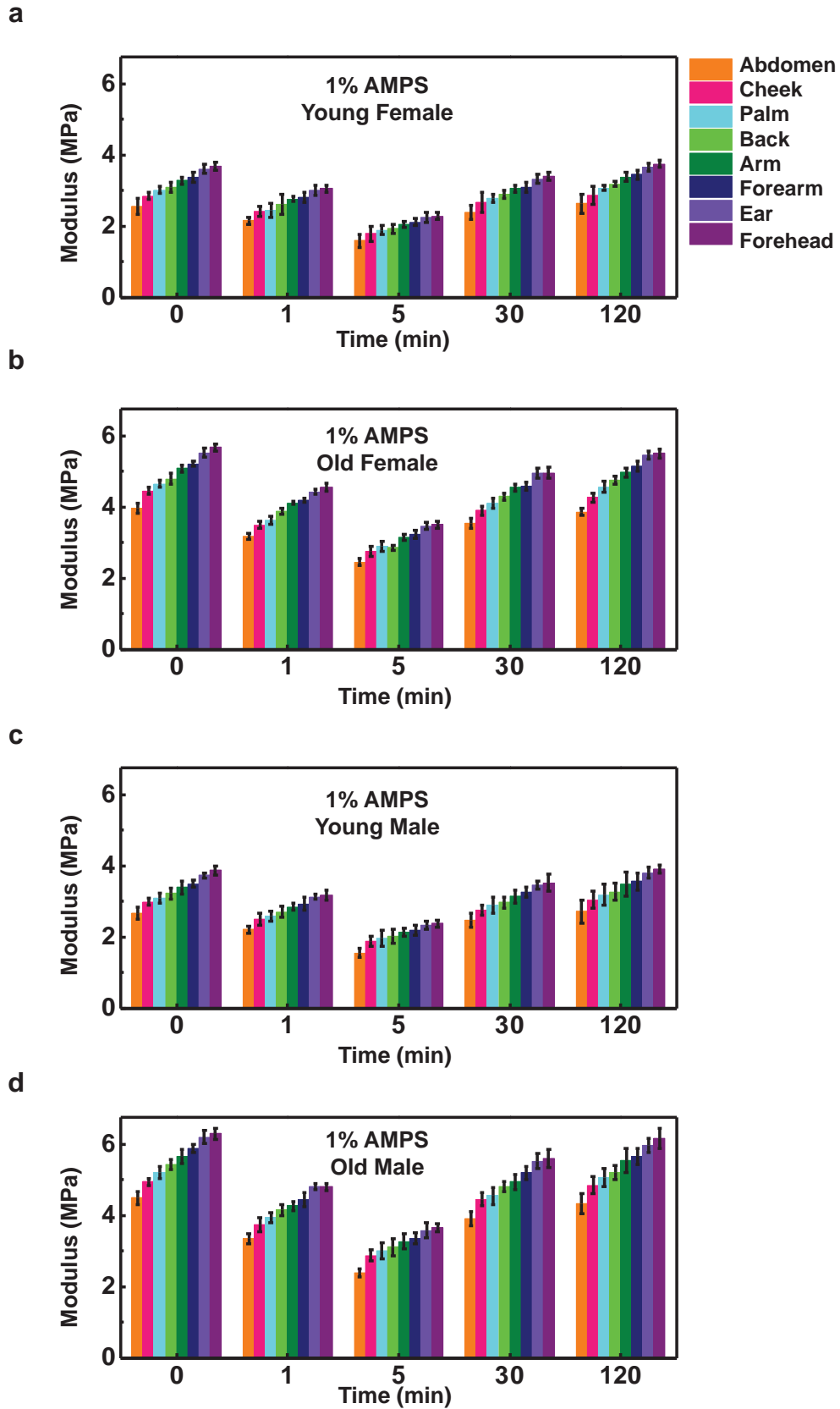
Supplementary Figure S20. *In vivo* evaluation of the modulus values of female and male skin before (0 min) and at various time points after the application of 1% AMPS solution. Modulus values for **(a)** young female, **(b)** old female, **(c)** young male and **(d)** old male skin on the abdomen, cheek, palm, back, arm, forearm, ear and forehead.
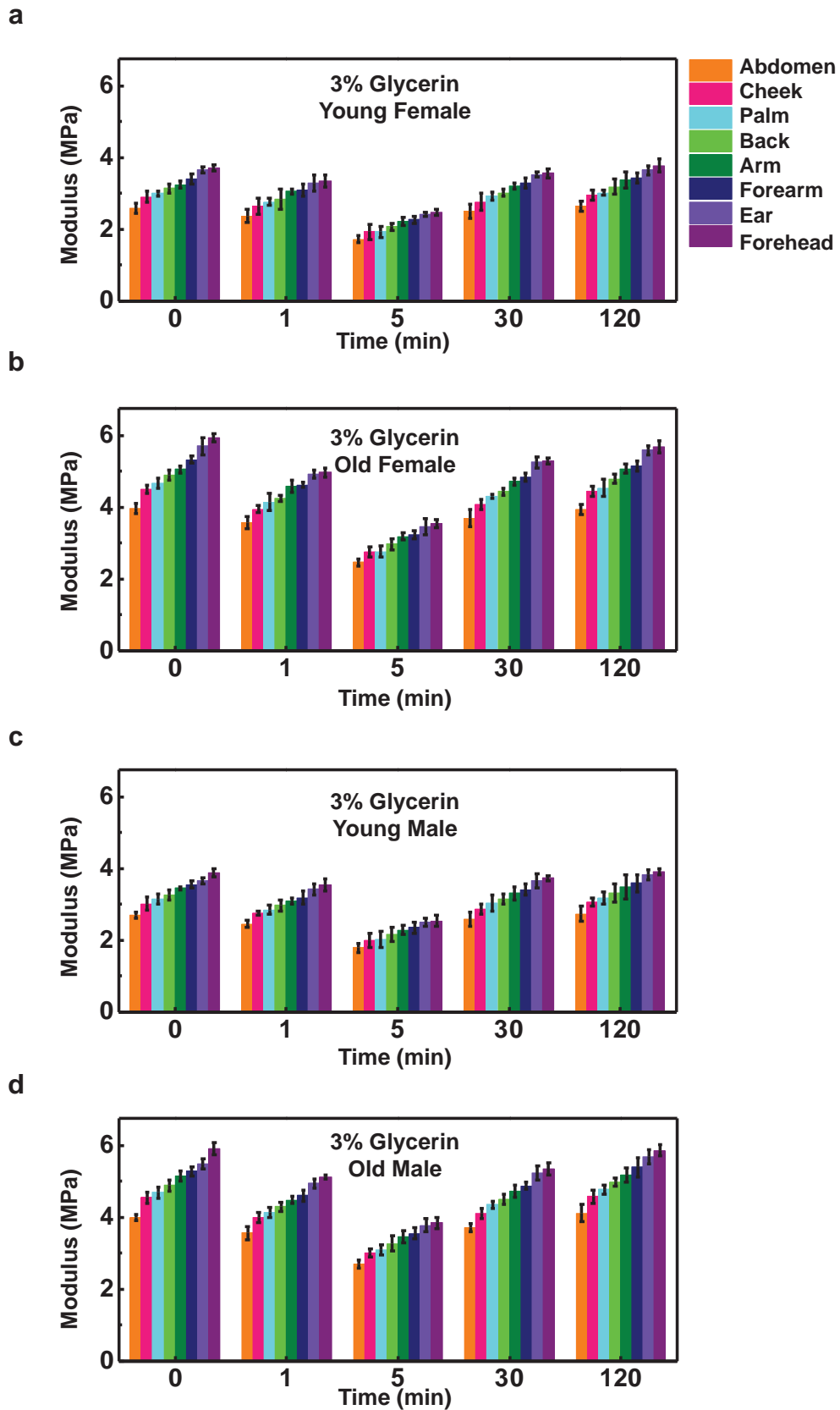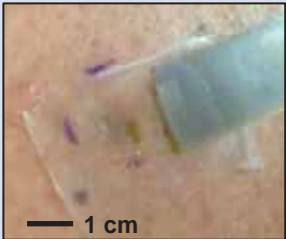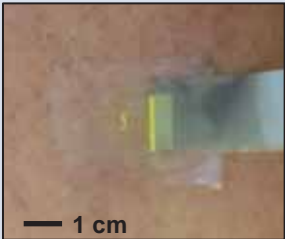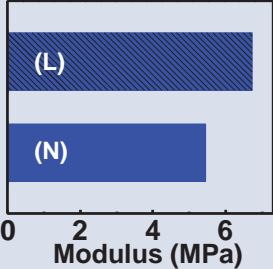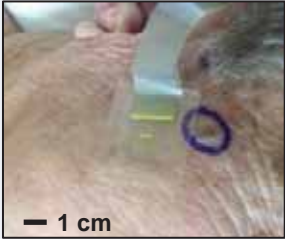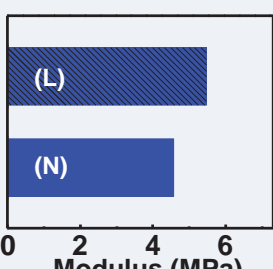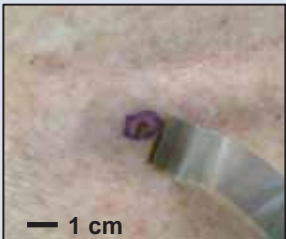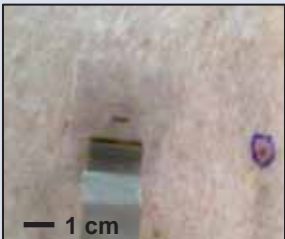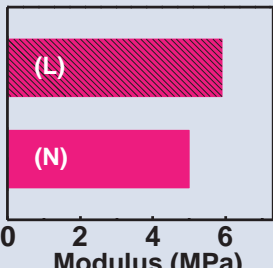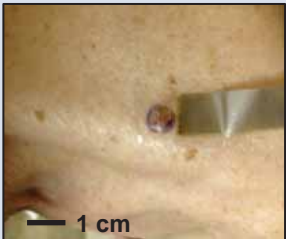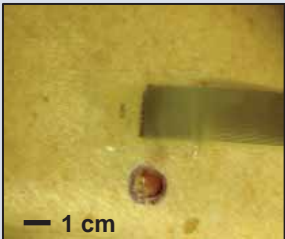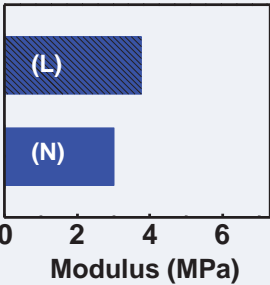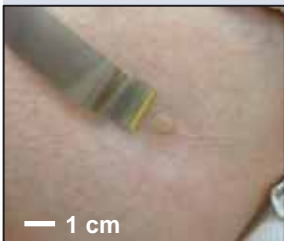
Supplementary Figure S21. *In vivo* **evaluation of the modulus values of female and male skin before (0 min) and at various time points after the application of 3% Glycerin solution.** Modulus values for **(a)** young female, **(b)** old female, **(c)** young male and **(d)** old male skin on the abdomen, cheek, palm, back, arm, forearm, ear and forehead.
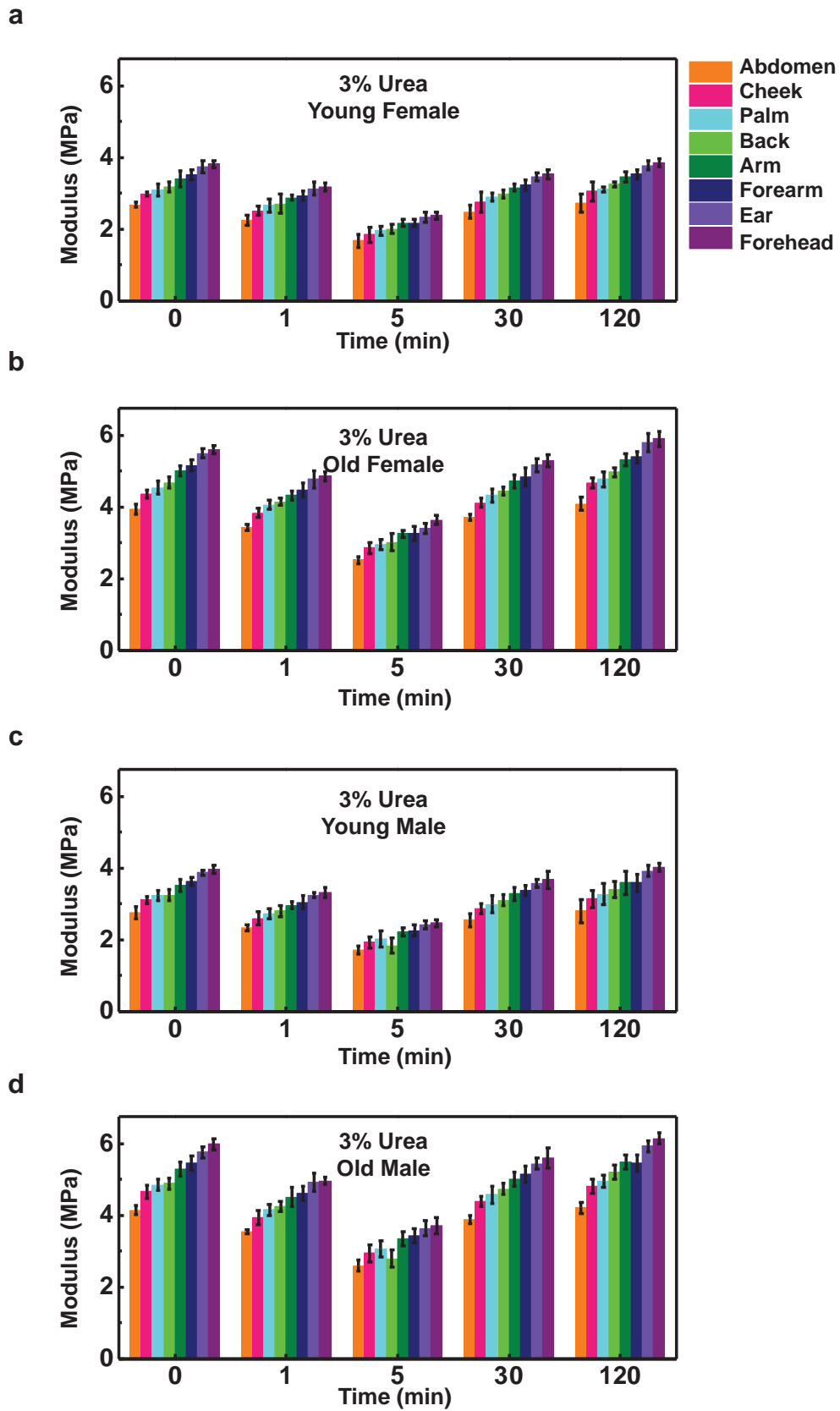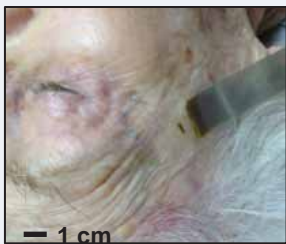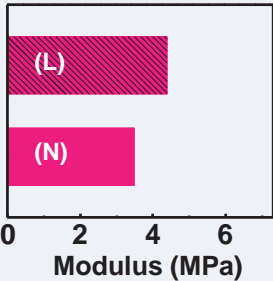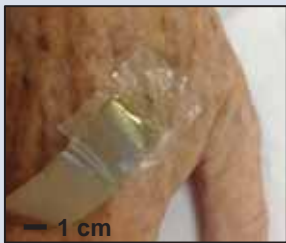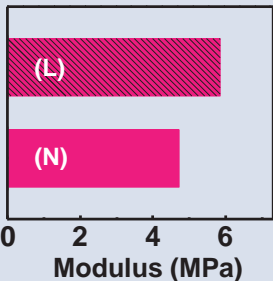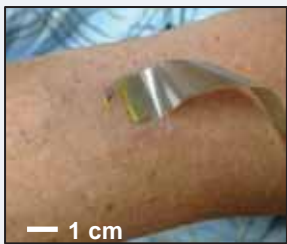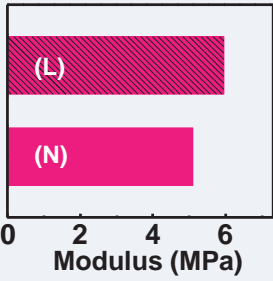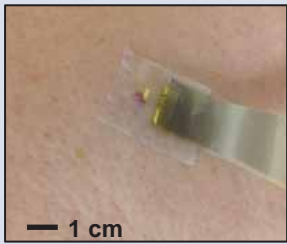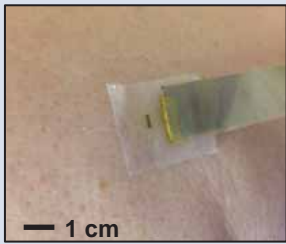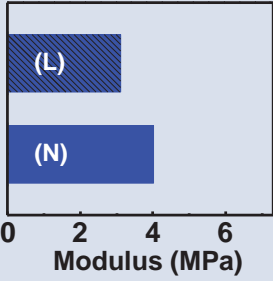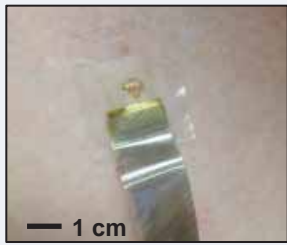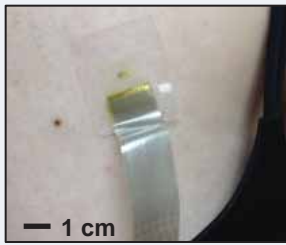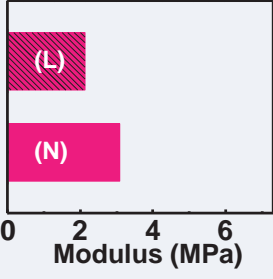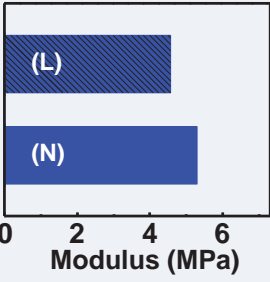
Supplementary Figure S22. *In vivo* **evaluation of the modulus values of female and male skin before (0 min) and at various time points after the application of 3% Urea solution.** Modulus values for **(a)** young female, **(b)** old female, **(c)** young male and **(d)** old male skin on the abdomen, cheek, palm, back, arm, forearm, ear and forehead.
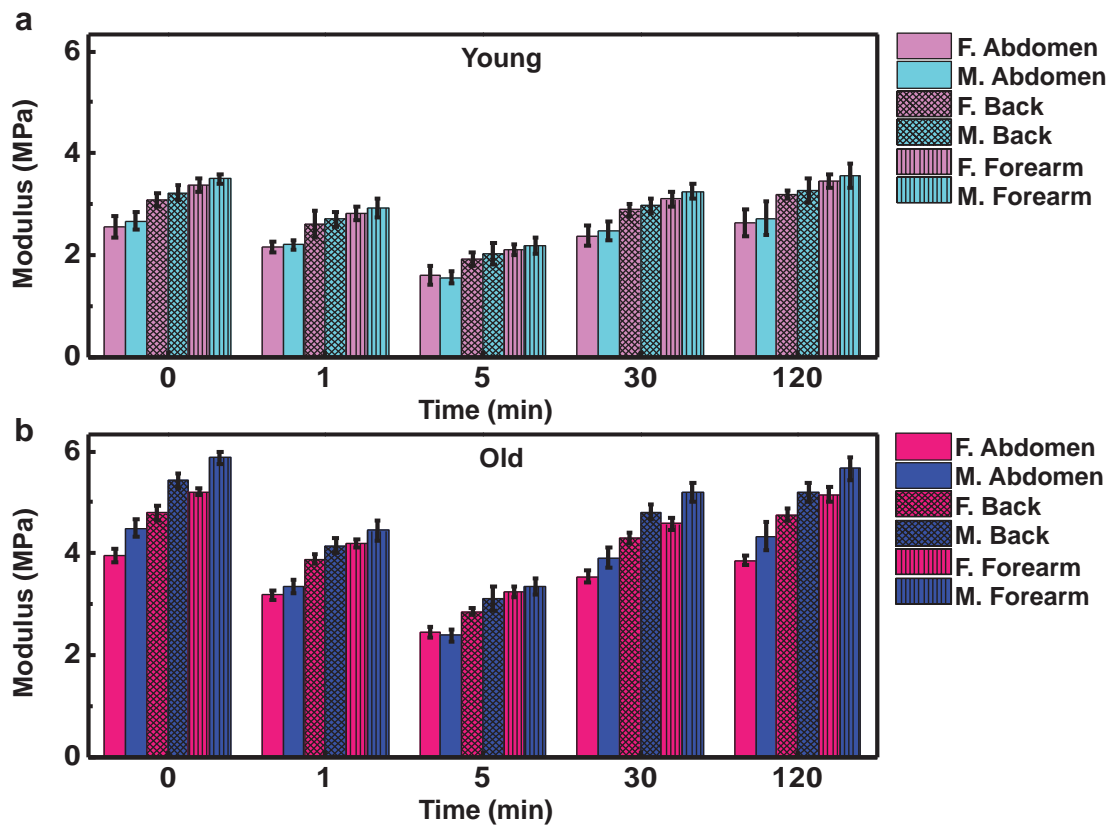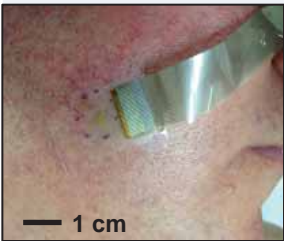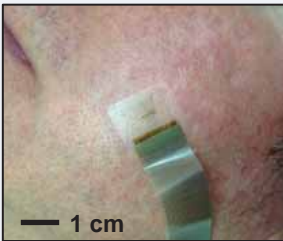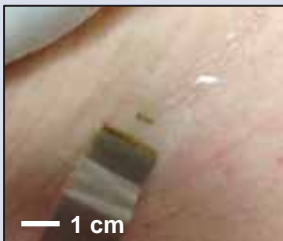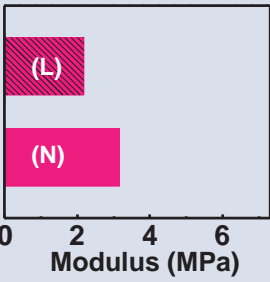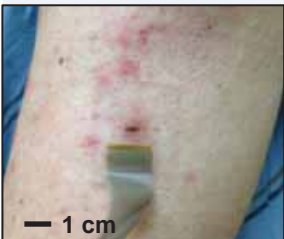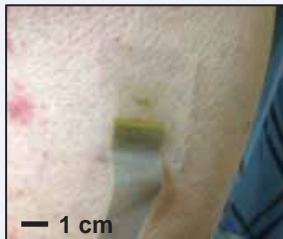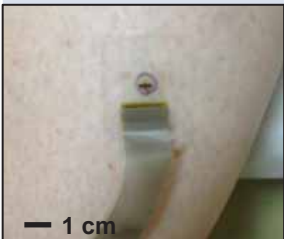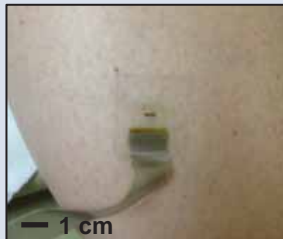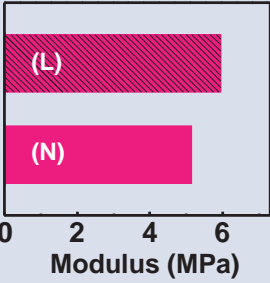
Supplementary Figure S23. *In vivo* **evaluation of the modulus values of female and male skin before (0 min) and at various time points after the application of 3% AMPS solution.** Modulus values for **(a)** young and (**b**) old skin.   Three skin locations for female and male cases are shown: F. vs. M. Abdomen (Female vs. Male Abdomen), F. vs. M. Back (Female vs. Male Back), F. vs. M. Forearm (Female vs. Male Forearm).

| LOCATION	LESION WITH DEVICE	BARE SKIN WITH DEVICE	DIAGNOSIS	RESULTS
(a) Back			fibrous histiocytoma	
(b) Temple			Seborrheic keratosis, irritated and inflamed	
(c) Back			Basal cell carcinoma	
(d) Armpit			compound nevus	
(e) Shoulder			basal cell carcinoma	

Supplementary Figure S24. *In vivo* modulus values obtained from various body locations along with photographs collected during the measurement for normal (N) and lesion (L) skin (Blue:Male, Pink:Female). **(a)** Back, **(b)** temple, **(c)** back, **(d)** ampit, **(e)** shoulder.

| LOCATION	LESION WITH DEVICE	BARE SKIN WITH DEVICE	DIAGNOSIS	RESULTS
(a) Temple			actinic keratosis	
(b) Hand			squamous cell carcinoma	
(c) Arm			seborrheic keratosis, irritated	
(d) Abdomen			irritated hemangioma	
(e) Breast			compound nevus	

Supplementary Figure S25. *In vivo* modulus values obtained from various body locations along with photographs collected during the measurement for normal (N) and lesion (L) skin (Blue:Male, Pink:Female). **(a)** Temple, **(b)** hand, **(c)** arm, **(d)** abdomen, **(e)** breast.

| LOCATION	LESION WITH DEVICE	BARE SKIN WITH DEVICE	DIAGNOSIS	RESULTS
(a) Cheek			Seborrheic keratosis, irritated and inflamed	
(b) Abdomen (under breast)			fibroepithelial polyp	
(c) Arm			superficial perivascular & interface lymphocytic dermatitis	
(d) Leg			severely atypical compound melanocytic proliferation	

Supplementary Figure S26. *In vivo* modulus values obtained from various body locations along with photographs collected during the measurement for normal (N) and lesion (L) skin (Blue:Male, Pink:Female). **(a)** Cheek, **(b)** abdomen (under breast), **(c)** arm, **(d)** leg.
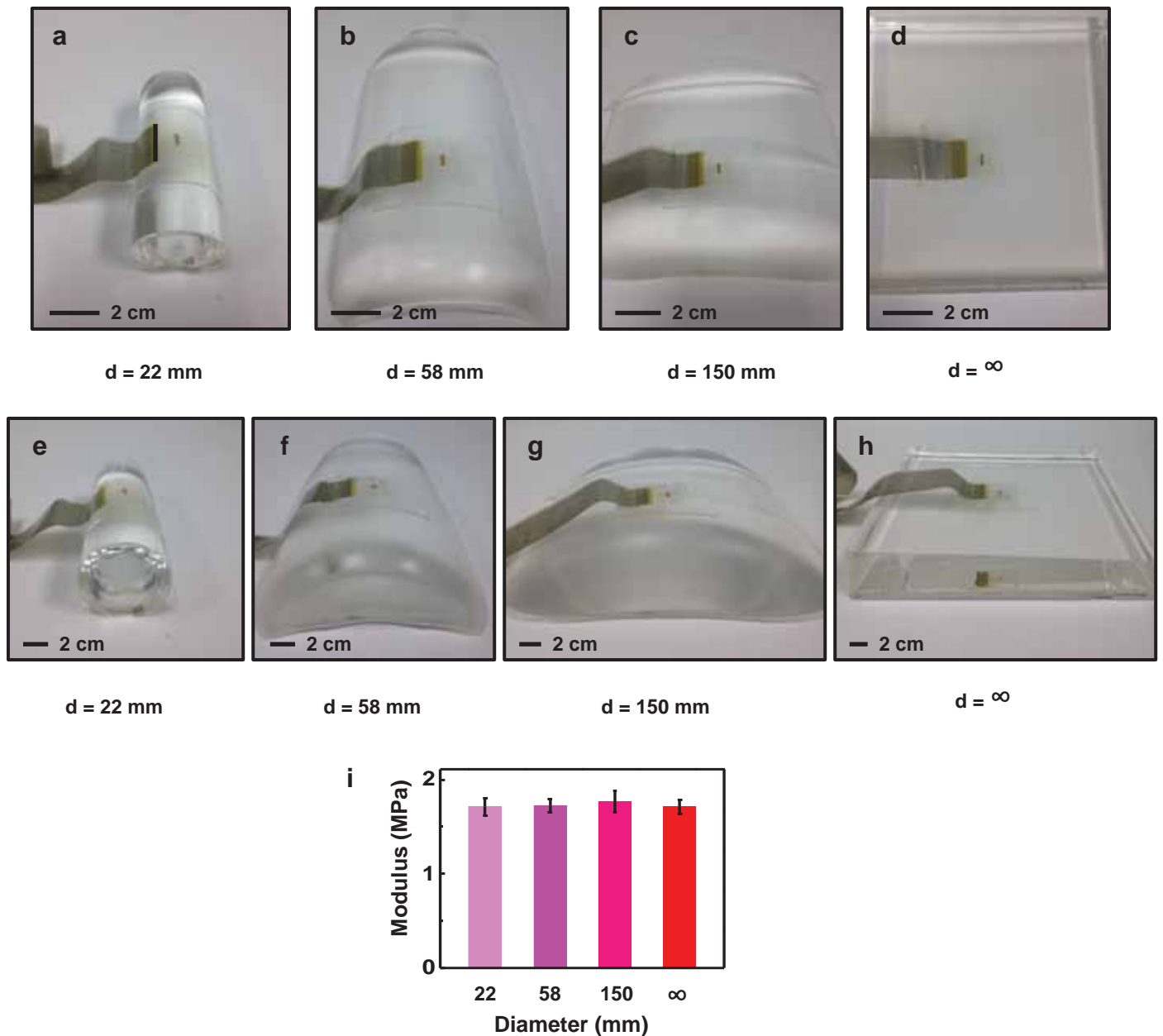
Supplementary Figure S27. Systematic studies of the effects of bending on the PZT CMS measurement. (a-d) Top view and **(e-h)** cross-sectional view of devices on cylindrical substrates of PDMS with diameter of curvature of 22 mm, 59 mm, 150 mm, and ∞, respectively. **(i)**. Sensor voltage and computed modulus values for PDMS substrate (E=1800 kPa) with various diameters.
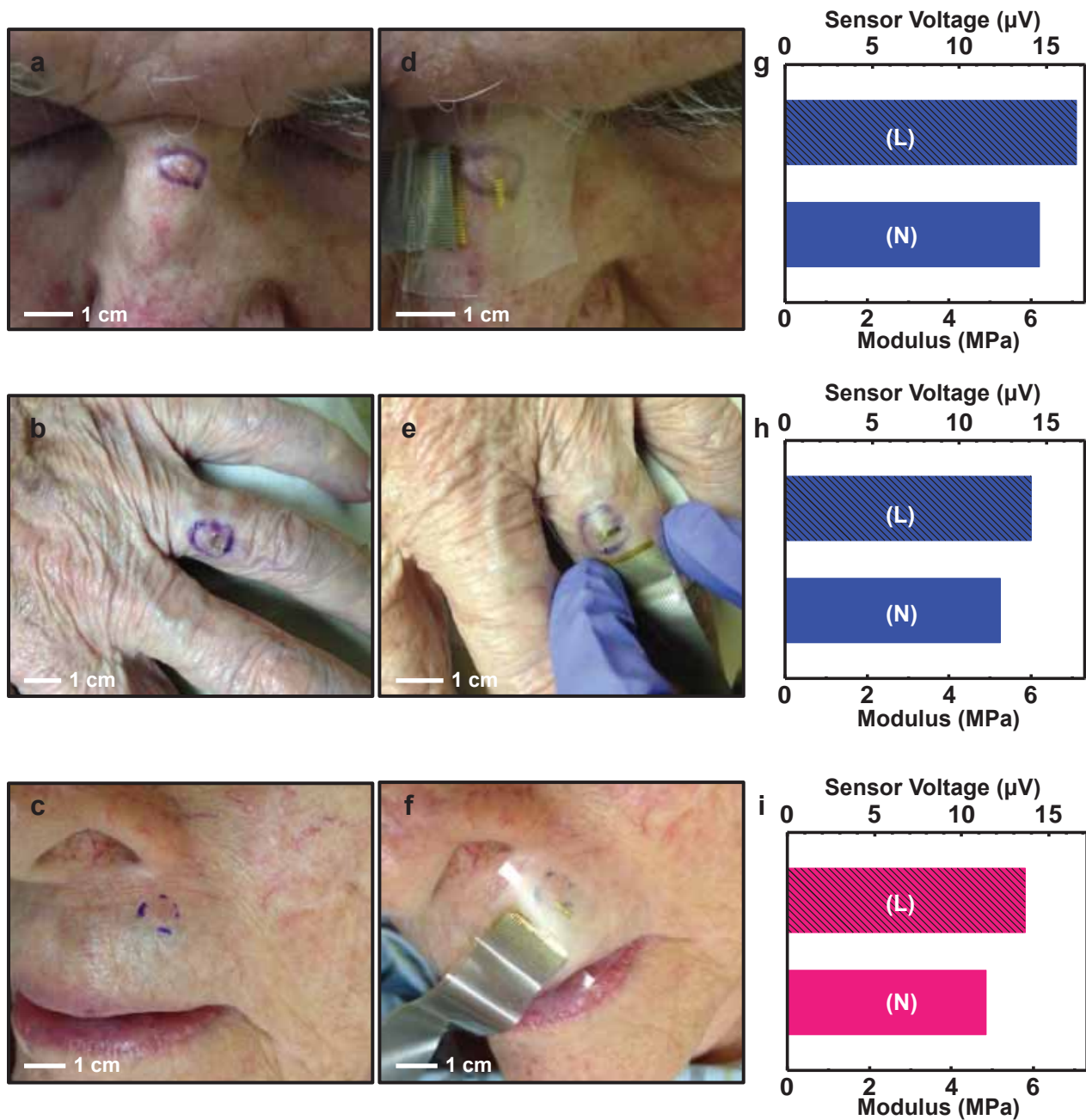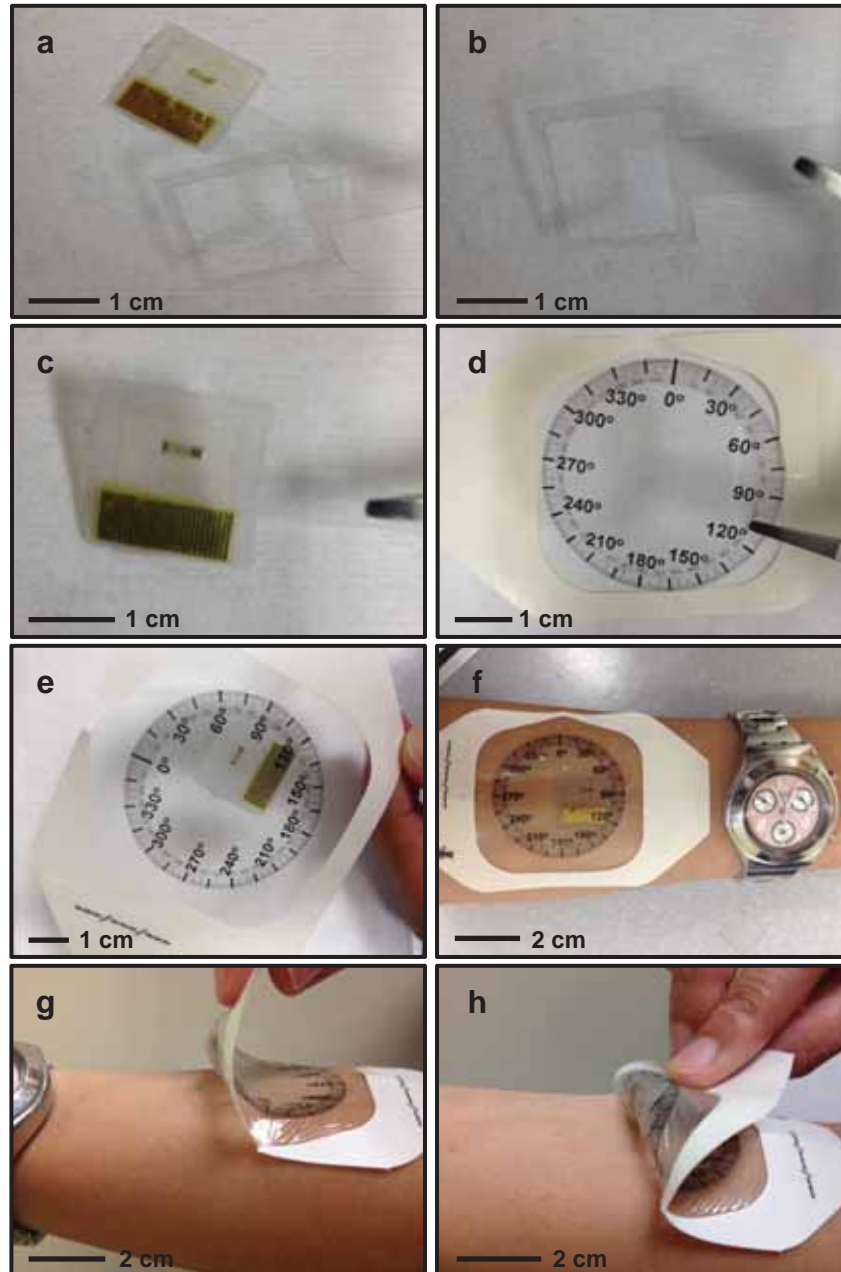
Supplementary Figure S28. Mapping of modulus values near and at the locations of basal cell carcinoma on the forehad and hand. Photograph of **(a)** nose, **(b)** finger and **(c)** lips without PZT CMS. Photograph of **(d)** nose, **(e)** finger and **(f)** lips with PZT CMS. **(g-i)** Modulus values extracted from the regions illustrated in the corresponding frames.
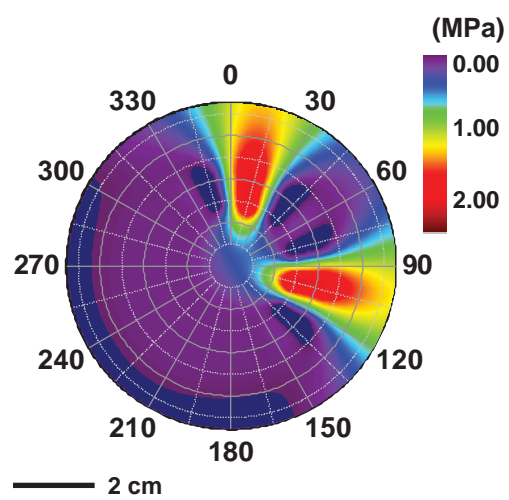
Supplementary Figure S29. Modulus values recorded with a rotatable PZT CMS system on a test sample of silicon rubber with high modulus regions between 0⁰ and 30⁰, 90⁰ and 120⁰.
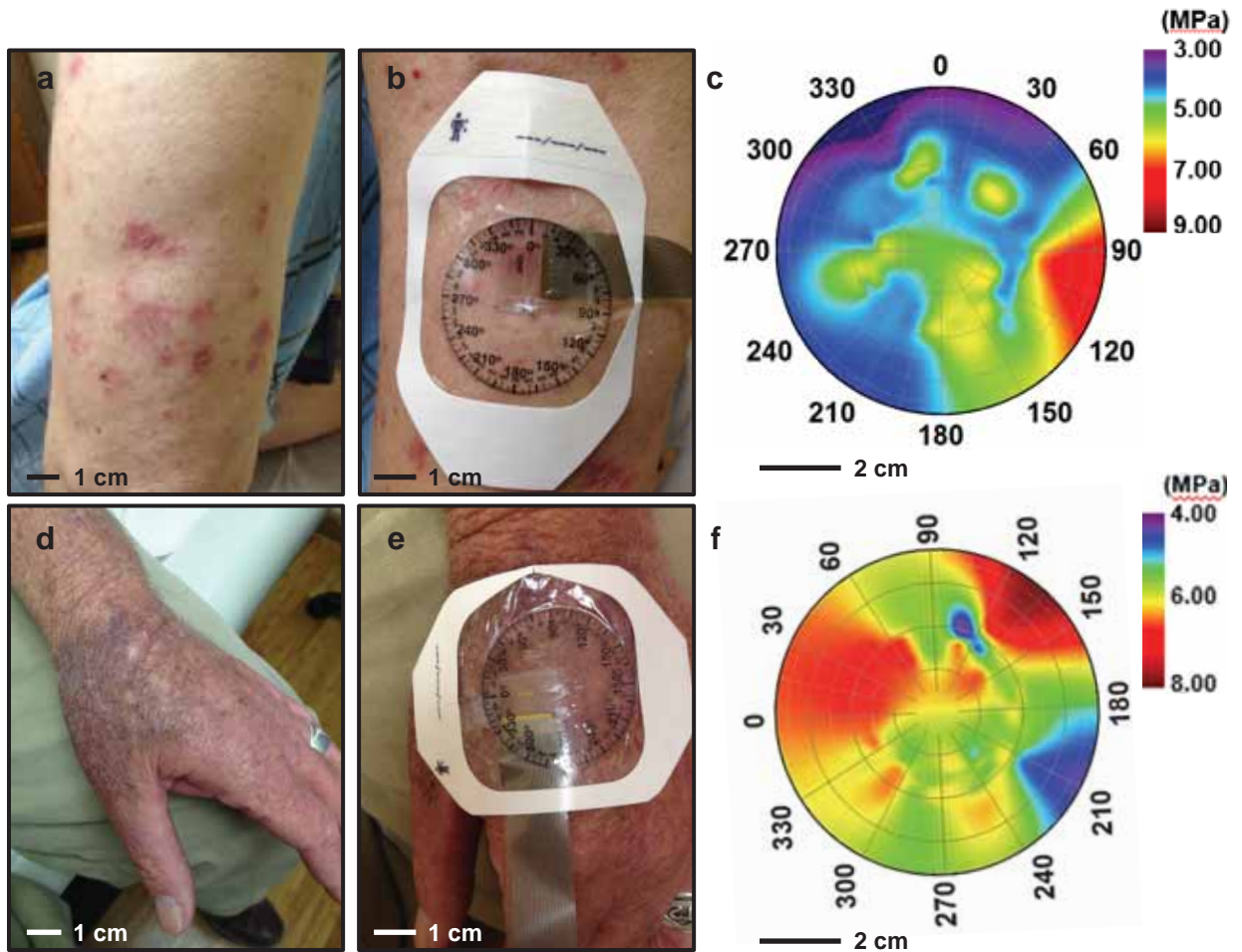
Supplementary Figure S30. Spatial map of modulus values collected from a region of the forearm that exhibits basal cell carcinoma. Photograph of the forearm **(a)** without and **(b)** with the rotatable PZT CMS device. **(c)** Map of modulus data recorded using the setup illustrated in **b**. Photograph of a hand **(d)** without and **(e)** with the rotatable PZT CMS device. **(f)** Map of modulus data recorded using the setup illustrated in **e.**

Supplementary Figure S31. Photographic illustration of steps for fabricating a rotatable PZT CMS device for spatially mapping the modulus. Photograph of **(a)** PZT CMS and window template, **(b)** window template, **(c)** PZT CMS on the window template, **(d)** protractor under a Tegaderm film, **(e)** PZT CMS protractor, **(f)** PZT CMS on the forearm, **(g,h)** peeling the PZT CMS protractor.
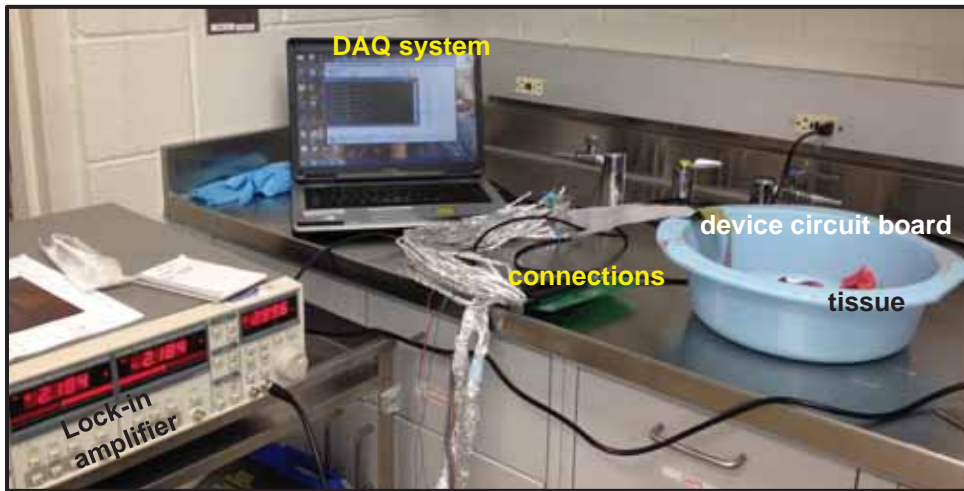
Supplementary Figure S32. PZT CMS system configured for measuring procured bovine organs.
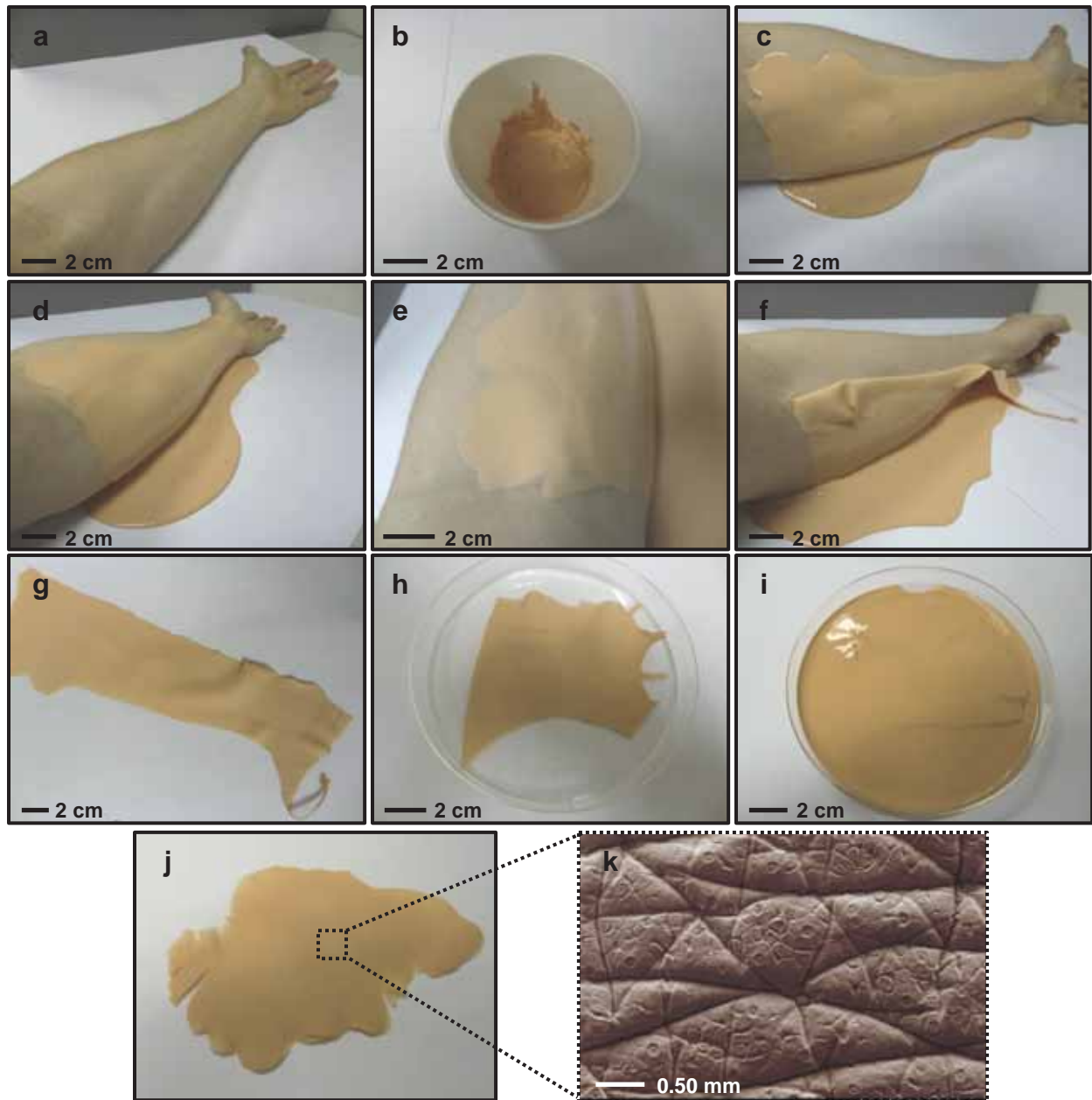
Supplementary Figure S33. Photographic illustration of the steps for preparing samples of artificial skin. (a) Bare skin without any treatment. **(b)** Mixture of dragon skin with silc pig. **(c-e)** Dragon skin placed on the forearm. **(f-g)** The cured dragon skin removed from the forearm. **(h)** A cut segment of dragon skin is placed in the petri dish. **(i)** The mixture of ecoflex with silc pig poured on the top of dragon skin sample. **(j)** Isolated segment of artificial skin. **(k)** SEM image of the black dashed region in **j**.
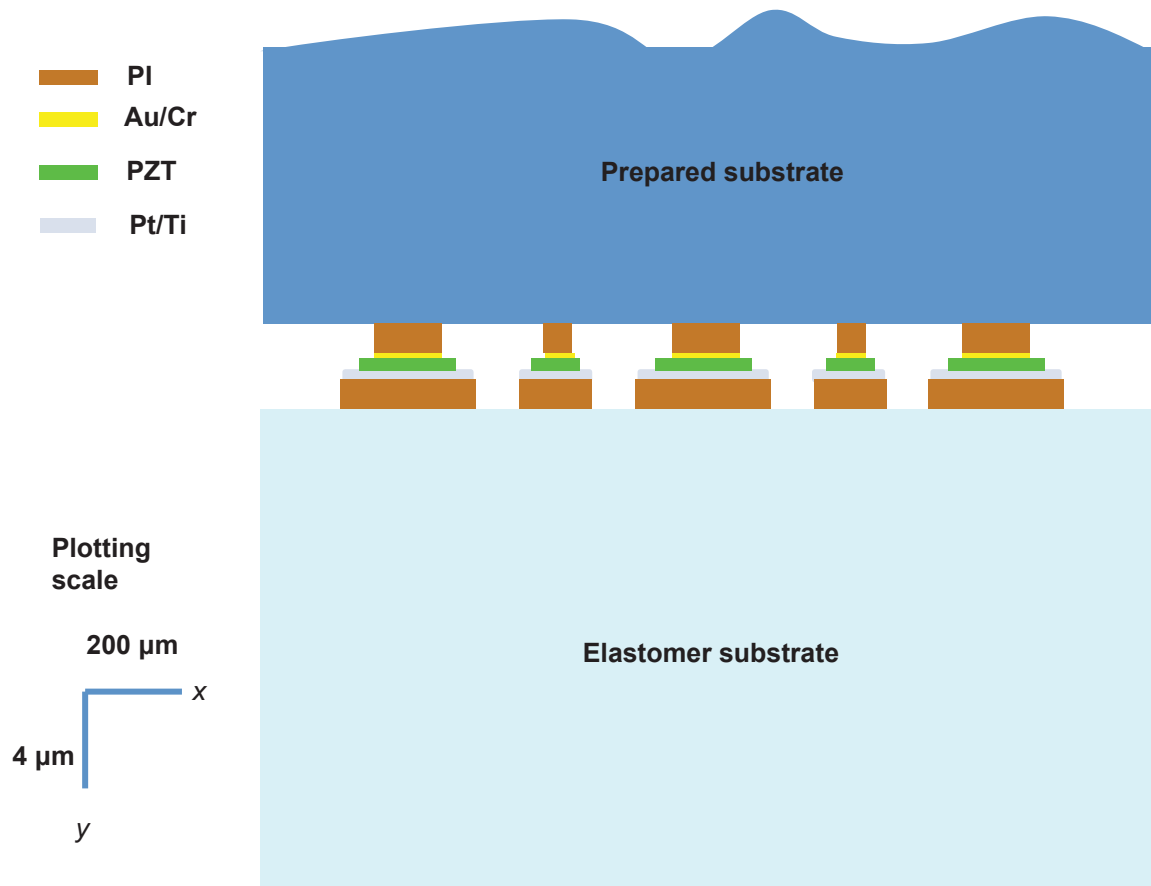
Supplementary Figure S34. Schematic cross sectional illustration of the multi-layer structure of the sensors/actuators, for the condition that the elastomer layer and prepared substrate do not adhered. The plotting scale in the vertical and horizontal directions are different as shown.

a

Subjects	E_{CMS}(MPa)	$E_{Indentation}$(MPa)
Young Female: 35-years old	2.7946±0.1924	130.3773±23.1960
Young Male: 33-years old	3.0108±0.1740	140.1820±16.5427
Old Female: 66-years old	4.4636±0.1320	163.2340±12.5963
Old Male: 69-years old	4.7164±0.1010	172.4880±22.8257

b

	Gender Male vs Female		Age Old vs Young	
	Young	Old	Male	Female
% variation for CMS	7.1808 ±0.1266	5.3600 ±0.0509	39.1631 ±0.0792	37.3913 ±0.0984
% variation for Nano indentation	6.9942 ±0.2959	5.365011 ±0.2095	18.7294 ±0.2503	20.1286 ±0.25551

Supplementary Table S1. (a) Modulus values of *ex-vivo* human abdominal skin using nanoindentation and CMS. **(b)** Percentage variations in moduli of *ex-vivo* human abdominal skin between genders and age using nanoindentation and CMS.

Reference	Sites	Young's Modulus (MPa)	Method
Silver *et al.*	Female* Male*	0.6 2.1	Tension
Stark *et al.*	Female* Male*	0.26 0.83	Tension
Diridollou *et al.*	Female -Forehead Male-Forehead Female-Forearm Male-Forearm	0.25 0.21 0.12 0.11	Suction
Barel *et al.*	Female-Forearm Male-Forearm Female-Forehead Male-Forehead Female-Temporal Male-Temporal	0.16 0.14 0.32 0.25 0.31 0.20	Suction
Sanders	Female-Forearm Male-Forearm	0.037 0.032	Torsion
Levequ *et al.*	Female-Forearm Male-Forearm	1.2 4.3	Torsion
This study	Female-Forearm Male-Forearm	3.41 3.55	CMS

* The site of the skin is not mentioned.

Supplementary Table S2. Variation in skin (human) modulus between genders as measured by CMS and various techniques from literature.